

行政院國家科學委員會專題研究計畫 期中進度報告

三維顆粒及流體運動之實驗與數模研究(1/3)

計畫類別：個別型計畫

計畫編號：NSC93-2211-E-002-020-

執行期間：93年08月01日至94年07月31日

執行單位：國立臺灣大學水工試驗所

計畫主持人：楊德良

共同主持人：卡艾璋

計畫參與人員：權順忠

報告類型：精簡報告

處理方式：本計畫可公開查詢

中 華 民 國 94 年 5 月 19 日

摘要

此報告為三年計畫中第一年的期中報告，此三年計畫為三維顆粒及流體運動之實驗與數模研究，在本研究中包含實驗方法與數值模擬方法。在實驗方法方面，第一年計畫包含：1-三維方形穴室中流體運動之量測。2-固體粒子交互作用時，周圍流體運動之三維量測。(包含粒子與粒子接近及碰撞)。3.在多固體粒子實驗中，兩種不同技術之比較。其中一種技術為雷射標記粒子之三維立體追蹤，另外一種技術是基於雷射光暈之單一影像。在計算方法方面，第一年包括：1.三維穴室流之計算。2.固體圓柱在流體運動之二維慣性及渦度計算。

Summary

The present report concerns the first year of a three-year research on liquid-granular flows. The research involves both experimental and computational methods. The experimental work conducted over the first year includes: 1) 3D particle trajectory measurements in a lid-driven cavity flow; 2) 3D measurements of liquid motions around interacting solid spheres (including sphere-sphere collisions and close encounters); 3) the comparative study of two different techniques for experiments involving many solid particles: one technique based on stereo tracking of laser-marked particles, and the other based on monoscopic imaging of laser halos. The computational work conducted over the first year includes: 1) 3D computations of the velocity field in the lid-driven cavity; 2) 2D computations of inertia and vorticity effects associated with the motion of solid cylinders in a liquid.

Experimental and computational study of 3D motions in liquid-granular flows

NSC Mid-term progress report, May 2005

1. Background and aims

The present report summarizes the progress made over the first year of a three-year research programme. The overall aim of the programme is to study 3D fluid and particle motions in liquid-granular flows using novel experimental and computational approaches.

Encountered in a variety of engineering applications, liquid-granular flows involve interactions between a carrier liquid and a dispersed granular phase. Debris flows, sediment-laden currents, and dredging slurries constitute examples of great practical concern. Such flows are difficult to study because they are inherently three-dimensional at the granular scale, since they strongly couple the solid and liquid phases, and therefore both the inertia and vorticity of the liquid play a crucial role.

To approach these phenomena, the project builds on experimental and computational methods developed recently in our laboratory. The experimental techniques designed specifically to study 3D liquid-granular flows include four components: 1) special testing apparatus including a recirculating rectilinear shear flow flume; 2) refractive-index matched liquid and granular materials allowing optical access to the flow interior; 3) capture of both liquid and granular motions through laser illumination of seeding particles and laser marking of granular cores; 4) image analysis algorithms allowing quantitative measurements of 3D motions. Numerical methods, on the other hand, include 3D Navier-Stokes computations in the velocity-vorticity formulation, and simulations of multi-body dynamics immersed in a liquid modelled by meshless calculations.

Over the three years of the programme, the objective is to examine liquid-granular flows in configurations of gradually increasing complexity. The specific results that were expected for the first year include:

- Detailed flow measurements for evolving configurations of a few spheres;
- Detailed measurements of many-particle motions in fluidisation cell tests;
- Detailed measurements of particle trajectories in lid-driven cavity flow experiments;
- Computations of passively advected particles in 3D flows;
- 2D and 3D potential flow computations of multi-body dynamics in a liquid bath.

These objectives have for the most part been met. Although delays have been encountered in certain areas, for others the objectives have already been exceeded, and the programme is on track to achieve its overall aims. The following sections outline the specific results obtained until now and the next steps that are being contemplated.

2. Experimental work

The experimental work conducted over the first year has focused on three areas: 1) detailed measurements of particle trajectories in lid-driven cavity flow experiments; 2) measurements of evolving configurations of a few spheres bathed in a liquid; 3) measurements of evolving configurations of many spheres in a liquid. Progress made in these three areas is presented in the next subsections.

2.1. Long time particle trajectories in lid-driven cavity flow experiments

Lid-driven cavity flow experiments performed using the apparatus illustrated on Fig. 1, were used to measure the long time trajectories of neutrally buoyant particles of finite size in a closed flow presenting a strong three-dimensional structure.

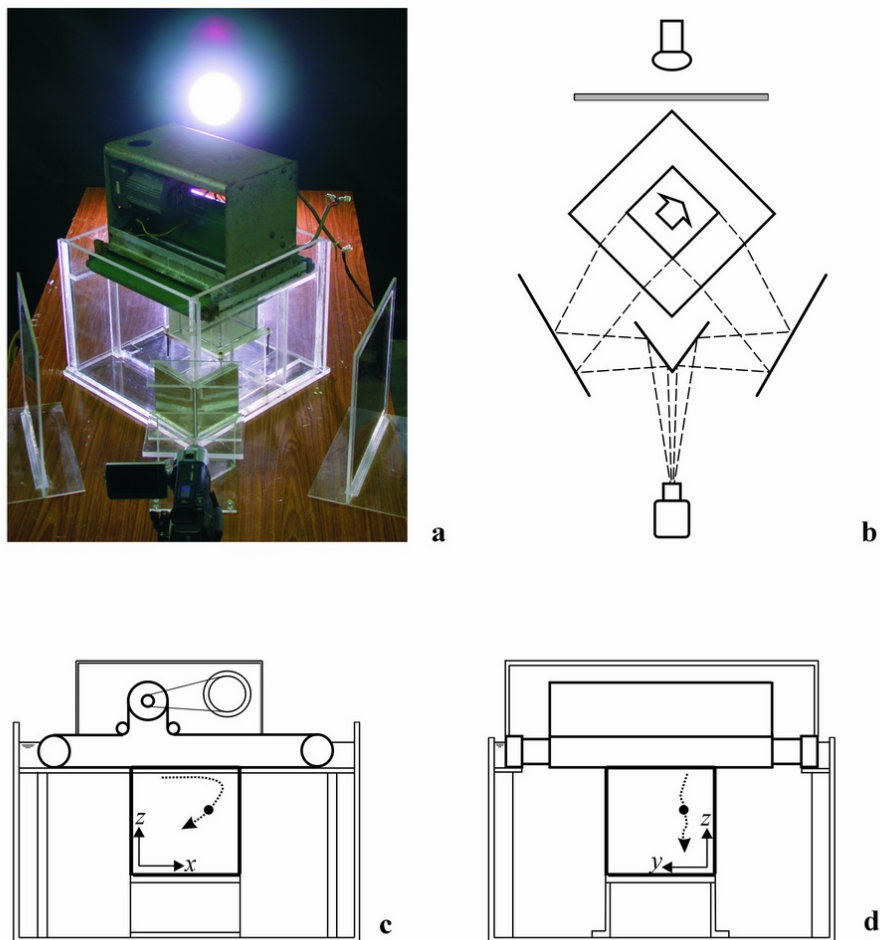


Figure 1. Lid-driven cavity used to probe particle motions in a 3D flow of a viscous liquid.

To obtain such measurements, stereoscopic imaging techniques are combined with Kalman filters, generating detailed time series of particle positions as they follow complicated orbits within the cavity. Such time series are shown on Fig. 2 for the three evolving spatial coordinates of a single particle.

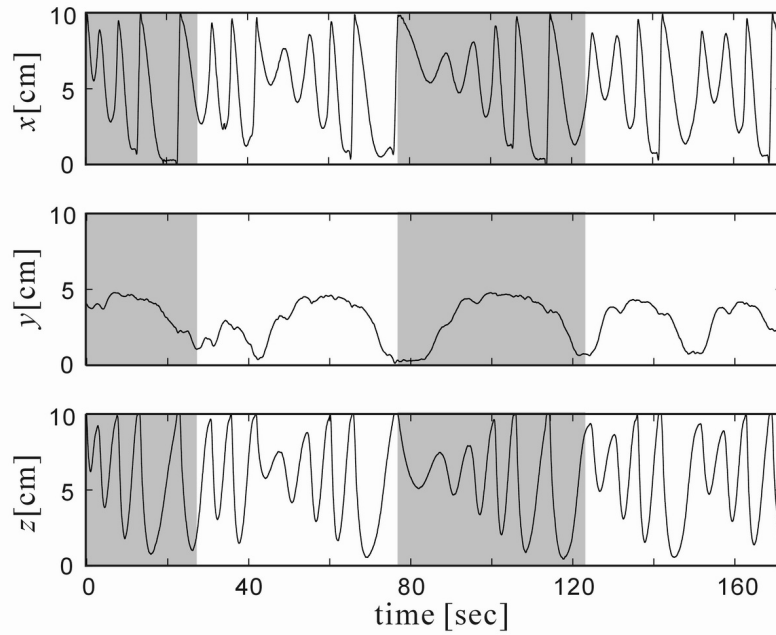


Figure 2. Measured time series of the 3D position of a single particle in the lid-driven cavity.

A 3D view of one representative orbital cycle (corresponding to the second period highlighted in gray on Fig. 2) is shown on Fig. 3. The figure shows a particle spiraling inwards and outwards along a path that reflects the internal circulation pattern of the liquid flow.

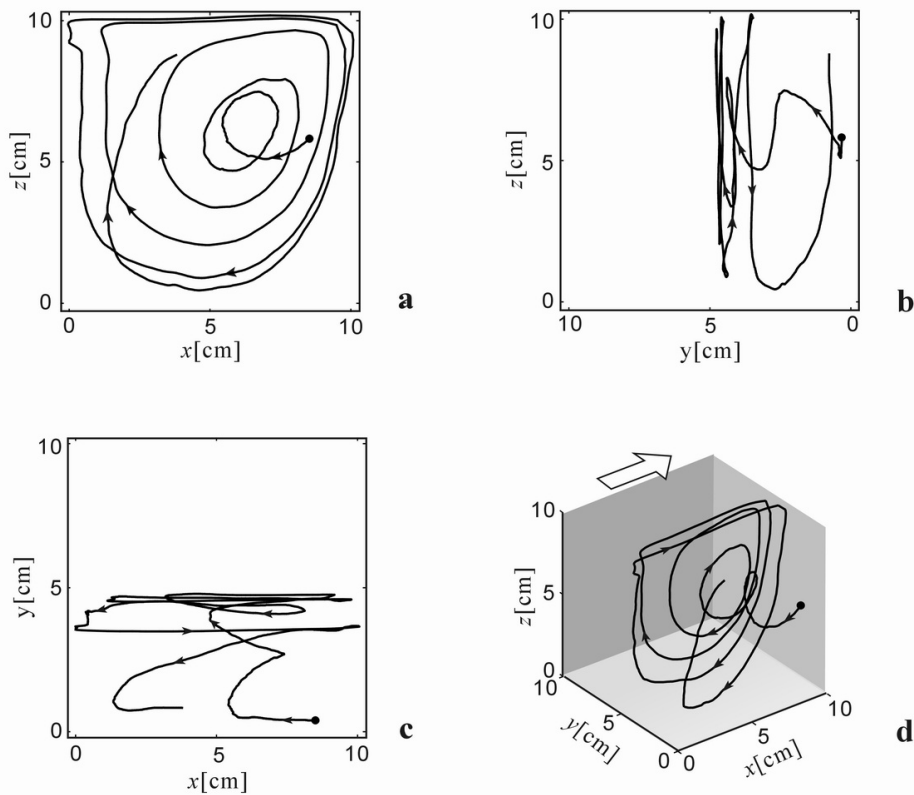


Figure 3. Segment of the 3D orbit of a single particle inside the lid-driven cavity.

Similar measurements were obtained for a variety of Reynolds numbers, and for flows involving various numbers of particles. An example involving the simultaneous motions of 10 particles in the cavity is shown in Fig. 4. The novel imaging and filtering approach used to obtain these measurements is documented in a paper recently submitted to the journal *Experiments in Fluids* (Tsorngr et al., submitted; see appendix).

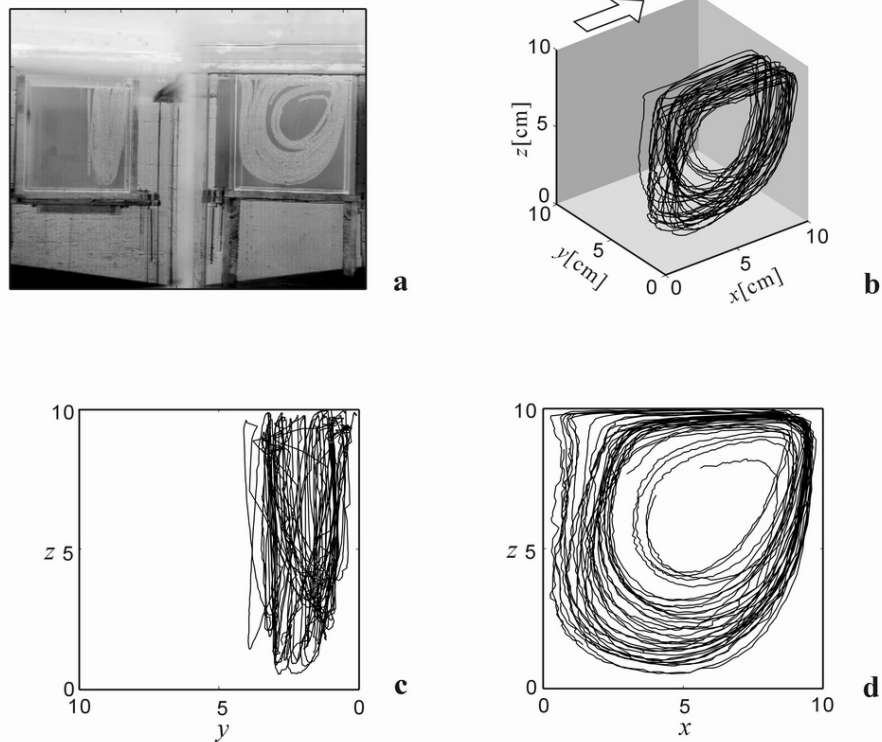


Figure 4. 3D orbits of 10 particles in the lid-driven cavity.

Work currently in progress aims to compare these measured trajectories with simulated trajectories reconstructed from numerical simulations. These are conducted using computational algorithms documented in a paper recently published in the *International Journal of Numerical Methods in Fluids* (Lo et al., 2005; see appendix).

2.2. 3D liquid motions around moving spheres

A second component of the experimental work conducted in the first year concerns liquid motions driven by moving spheres. Such motions are examined using the approach illustrated on Fig. 5. Large transparent spheres are bathed in a liquid seeded with microparticles and illuminated by a laser light sheet. The objective is to capture both the sphere motions and the induced 3D motions of the liquid. The novel aspect of the approach is that the sphere and liquid materials have the same refractive index. This guarantees visual access from all angles and avoids laser illumination shadows and caustics that would otherwise hinder observation.

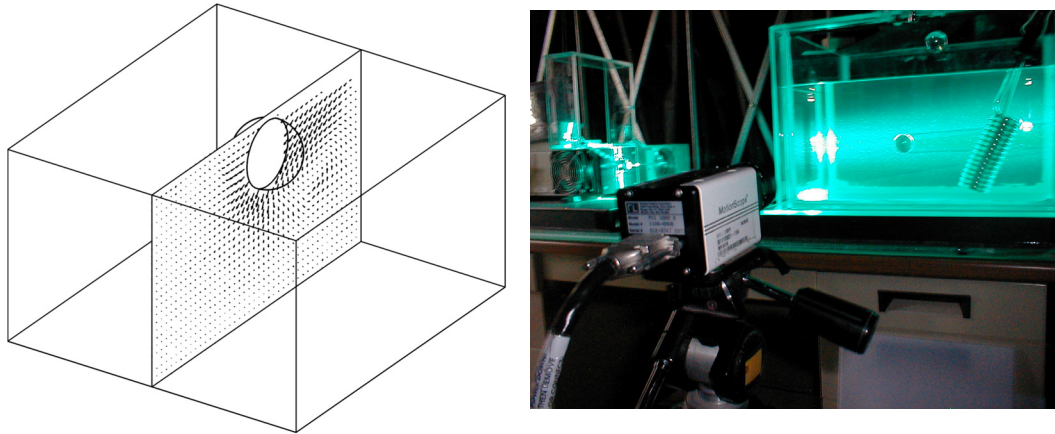


Figure 5. Laser illumination of liquid motions around transparent solid spheres of matched refractive index.

Long exposure image results in three different planes are presented on Fig. 6, for a case of a rapidly moving sphere passing next to an initially static sphere. Thanks to the refractive index matching approach, the seeding particles are illuminated and viewed throughout the field (including in the space between the two spheres). The sphere silhouettes show up as bright halos which can be tracked to reconstruct the sphere motions.

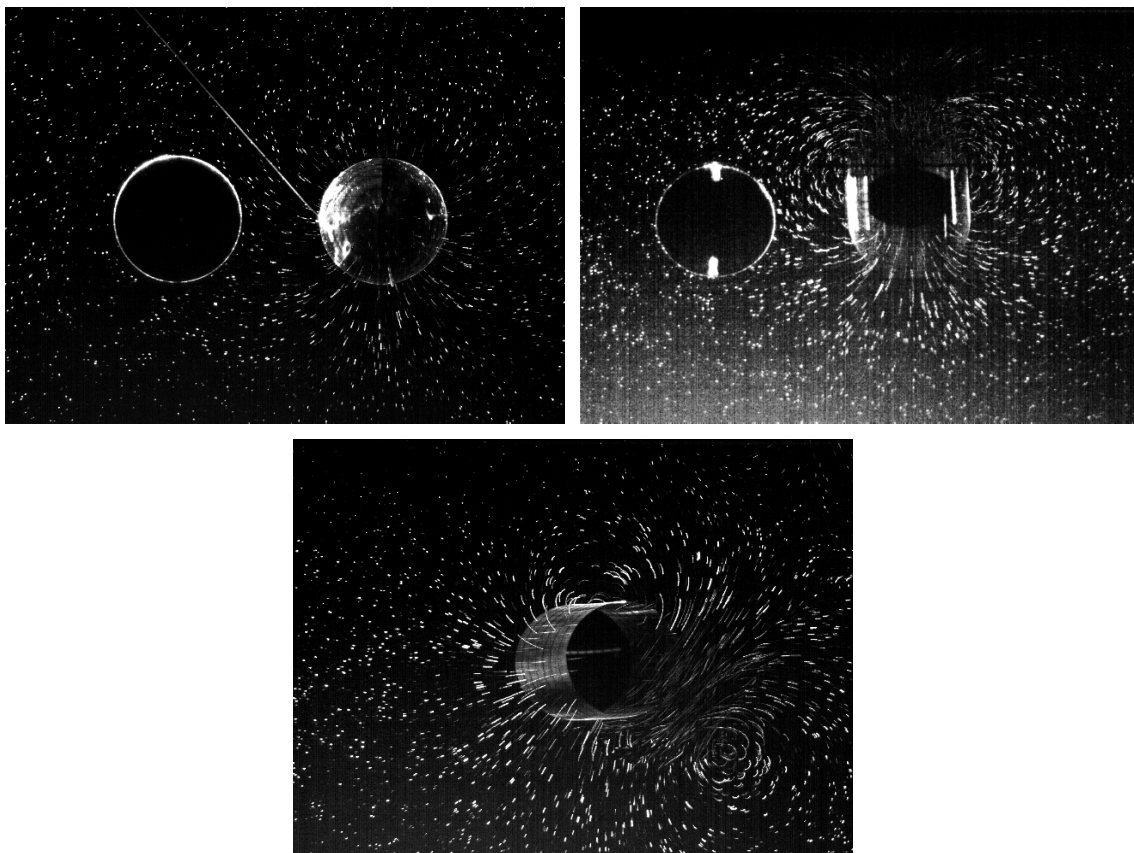


Figure 6. Long exposure views of close encounter between two spheres in a liquid. Top left: front view; top right: top view; bottom: side view.

The images of Fig. 6 constitute two-dimensional slices of a 3D flow field, and can be assembled into a 3D composite representation shown on Fig. 7. A vortex ring structure associated with the moving sphere can be seen. Starting from rest, the second sphere undergoes small amplitude motions due to the encounter.

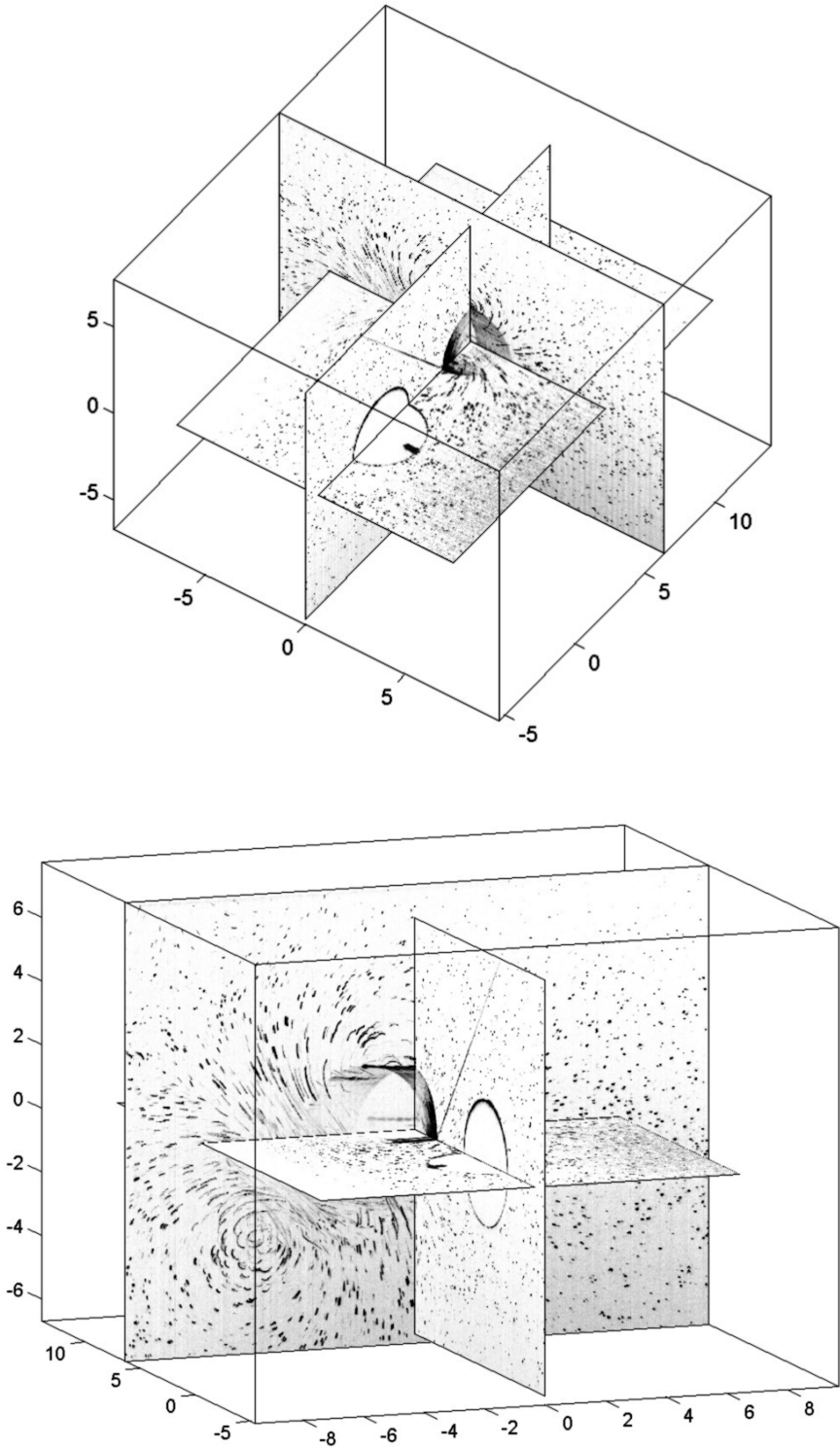


Figure 7. 3D assembly of the laser-illuminated planes shown on Fig. 6. Axis dimensions in centimeters.

2.3. 3D motions of systems of many solid particles in a liquid

The more ambitious objective of the overall research programme is to capture the 3D motions of systems of many solid particles bathed in a flowing liquid. Liquid-granular surges such as the one shown on Fig. 8 are of specific interest, due to their relevance to naturally occurring debris flows.

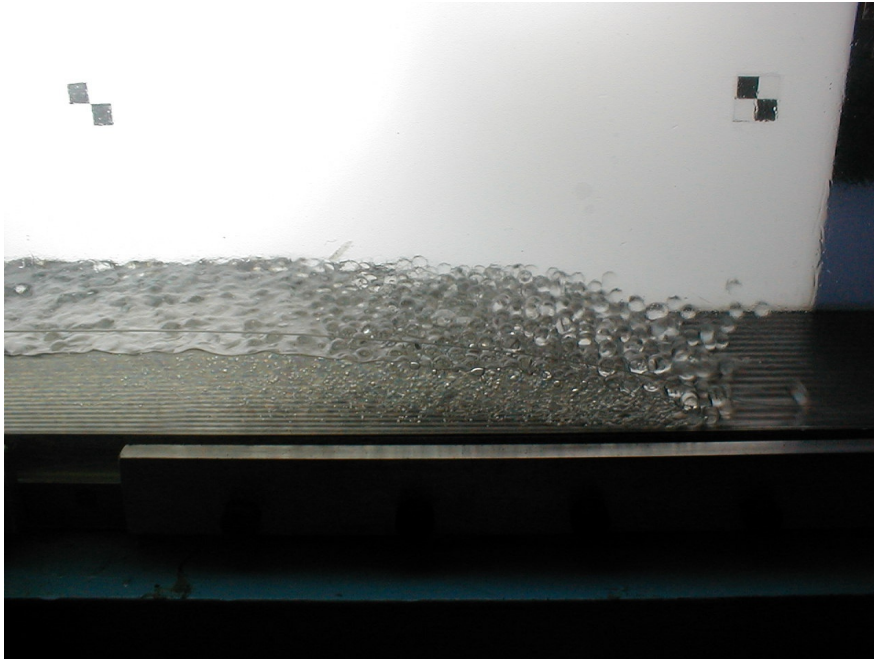


Figure 8. Front of a debris surge, composed of a mixture of para-cymene and acrylic beads.

Two approaches are contemplated to measure granular motions inside such complicated flows. The first approach, similar to the one used for the lid-driven cavity experiments of section 2.1, is based on stereoscopic imaging. To preserve visual access to the inside of a dense dispersion of grains, refractive index matching is again used, and combined with laser marking of particle cores. This technique was tested successfully for a dense dispersion of spheres in a fluidisation column, as illustrated on Fig. 9. Its extension to surges, such as the one shown on Fig. 8, is however in doubt due to various factors: 1) particle velocities are much greater than in the fluidization column; 2) visual access is restricted to sidewalls, hindering stereo viewing; 3) small air bubbles entrained at the front of the surge propagate for long distances into the flow: because the bubbles look similar to the laser-marked particle cores, confusion is likely.

Based on the work presented in section 2.2., we are currently exploring an alternative approach, based on cross-correlating particle halos as they pierce laser planes oriented perpendicularly to the flow. Attractive features of this technique are that: 1) higher velocities are possible, and 2) large grains and small particles (bubbles or seeding particles) can be distinguished from each other, as illustrated on Fig. 10. Work is currently in progress to test the feasibility of this approach. A major hindrance in this regard is that we are currently

lacking a laser illumination device of sufficient power.

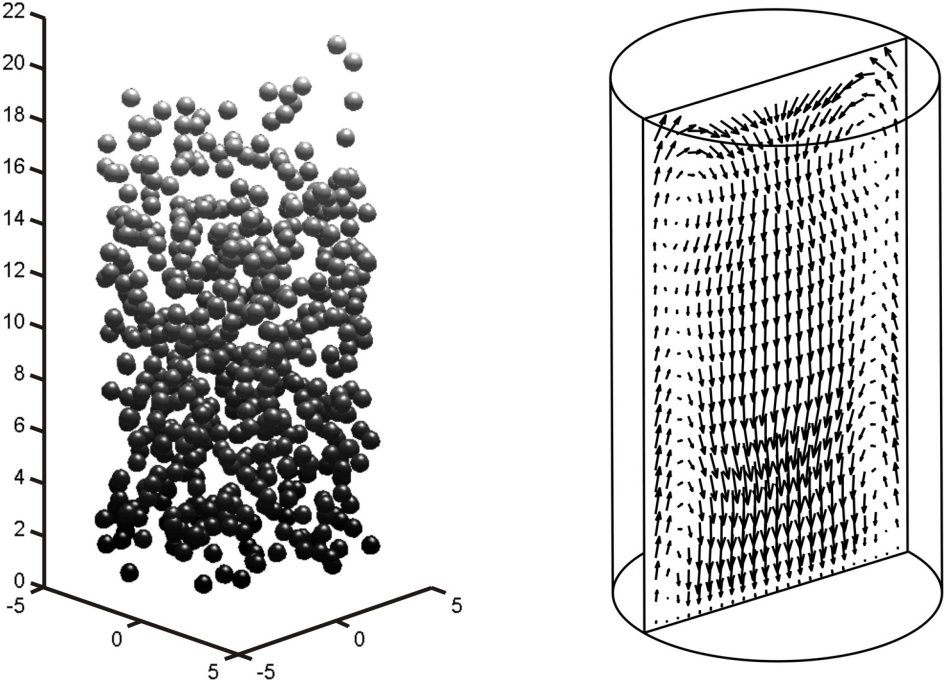


Figure 9. 3D granular positions and circulation pattern in a fluidisation column.

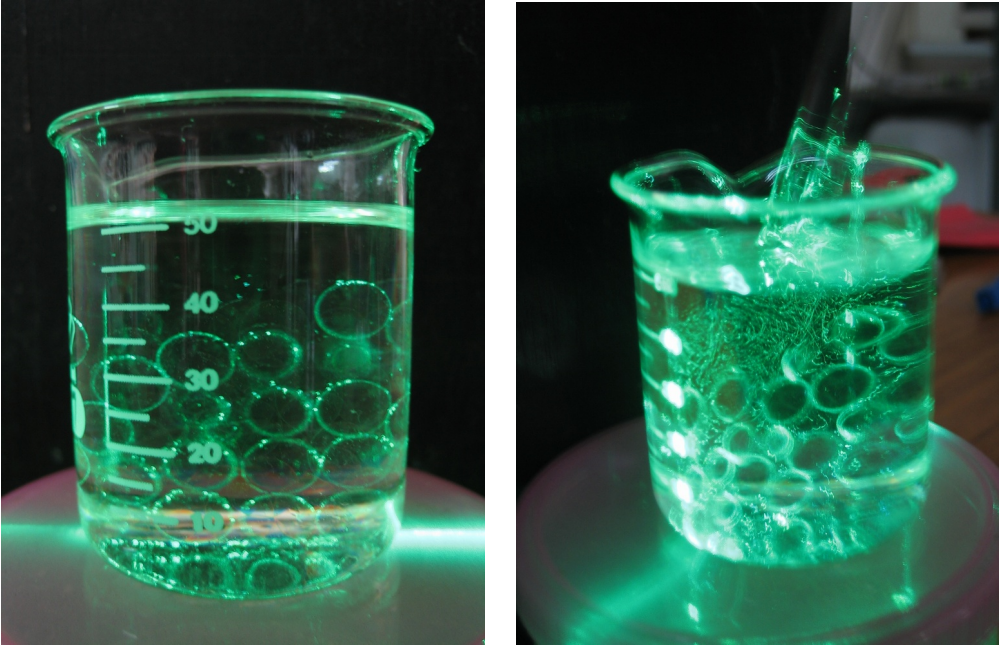


Figure 10. Alternative approach based on laser sheet illumination of granular halos.

3. Computational work

In parallel with the experimental work summarized in the previous section, progress has been made in three different areas of computational modeling: 1) Navier-Stokes computations of the 3D viscous flow field in the lid-driven cavity, including simulations of the trajectories of passively advected particles within this flow field; 2) computations of the dynamics of solid particles in irrotational flow fields; 3) computations of the dynamics of solid particles in flow fields with vorticity. Our work in the first area has reached a high degree of maturity, as documented in a paper recently published in the International Journal of Numerical Methods in Fluids (Lo et al., 2005; see appendix).

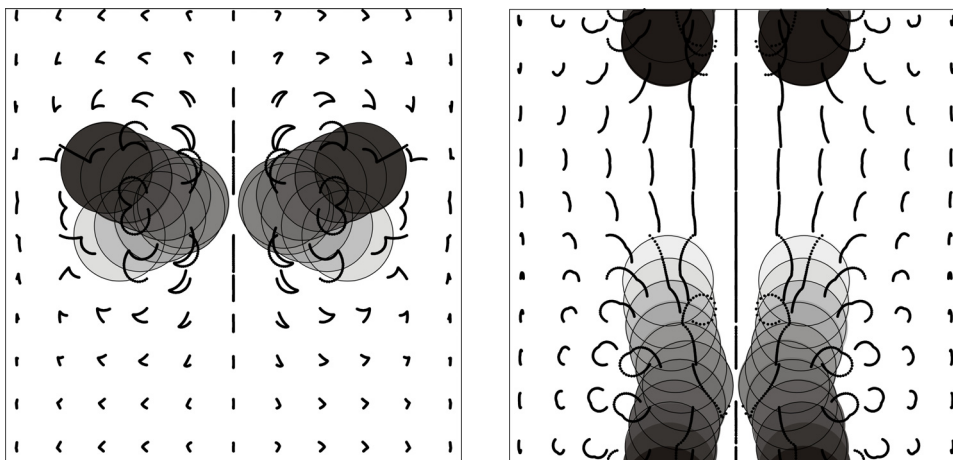


Figure 11. Symmetric motions of two massless particles in a liquid-filled periodic box (with associated pathlines of a set of liquid tracers).

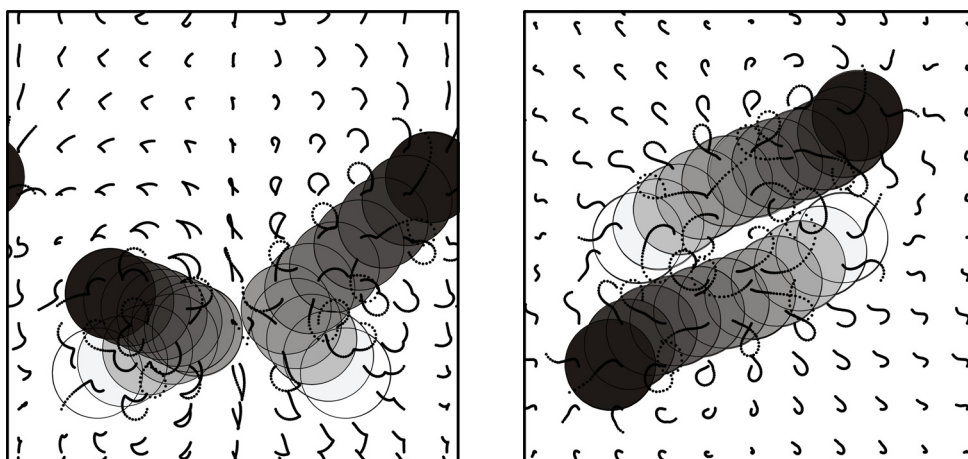


Figure 12. Asymmetric motions of two massless particles in a liquid-filled periodic box (with associated pathlines of a set of liquid tracers).

In the second area, two-dimensional computations have been obtained for a variety of configurations, including particle interactions inside a liquid-filled periodic box illustrated on Figs. 11 and 12. Some issues remain to be resolved, however, including questions of energy conservation, and extension to 3D has not yet been achieved.

For the third area, on the other hand, work has proceeded faster than scheduled, yielding results which exceed our initial expectations. For two-dimensional flow fields, vorticity effects have been successfully incorporated in computations of liquid-particle interactions by introducing discrete vortices in the flow field, and calculating their effects on solid cylinders. Preliminary results for simple configurations are illustrated on Figs. 13 and 14.

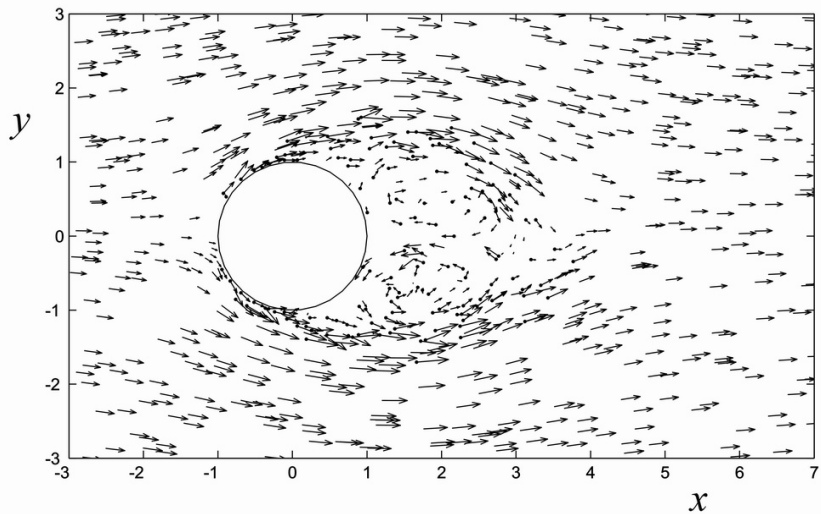


Figure 13. 2D flow field around a cylinder calculated using discrete vortices.

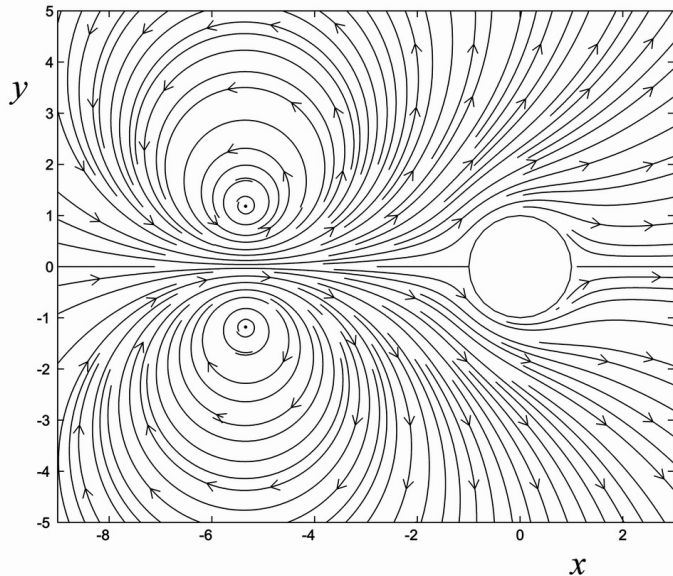


Figure 14. Instantaneous streamlines associated with a vortex pair interacting with a freely moving cylinder.

References (see appendixes)

- Lo, D.C., Murugesan, K., and Young, D.L. (2005) Numerical solution of three-dimensional velocity–vorticity Navier–Stokes equations by finite difference method. *Int. J. Numer. Meth. Fluids* **47**:1469–1487.
- Tsornng, S.J., Capart, H., Lai, J.S., and Young, D.L. (submitted) Three-dimensional tracking of the long time trajectories of suspended particles in a lid-driven cavity flow. Submitted to *Experiments in Fluids*.

Self-evaluation

The three year programme is to examine liquid-granular flows in configurations of gradually increasing complexity. The specific results that were expected for the first year include:

- 1) Detailed flow measurements for evolving configurations of a few spheres;
- 2) Detailed measurements of many-particle motions in fluidisation cell tests;
- 3) Detailed measurements of particle trajectories in lid-driven cavity flow experiments;
- 4) Computations of passively advected particles in 3D flows;
- 5) 2D and 3D potential flow computations of multi-body dynamics in a liquid bath.

Objectives 1) to 4) have been attained. For objective 5), some difficulties remain to be addressed before 3D flows can be tackled. In 2D, however, the objective has been exceeded: preliminary computations of vorticity effects have allowed us to go beyond potential flow, ahead of the original schedule. The programme is thus on track to achieve its overall aims.

Three-dimensional tracking of the long time trajectories of suspended particles in a lid-driven cavity flow

S.J. Tsorng^{1,2}, H. Capart^{1,2}, J.S. Lai² and D.L. Young^{1,2}

Abstract

Stereo imaging methods are used to measure the positions of solid spherical particles suspended in a viscous liquid and enclosed in a transparent cubic cavity. The liquid and particle motions are driven at the top lid by a conveyor belt operated at constant speed. Based on sequences of stereo views of the full cavity, the particles are tracked continuously along their three-dimensional orbits. The corresponding position histories are treated as noisy stochastic data and processed using Kalman filters to attenuate the effect of measurement errors. The lid-driven viscous flow is characterised by an intricate internal structure which is mirrored in the particle paths. Although the particles are neutrally buoyant, because of their finite size they are not merely advected by the liquid flow. Instead the long time trajectories tend to cluster along preferential pathways of the internal circulation pattern.

¹ Department of Civil Engineering, National Taiwan University, Taipei 106, Taiwan.

² Hydrotech Research Institute, National Taiwan University, Taipei 106, Taiwan.

1

Introduction

A wide variety of experiments involve moving particles embedded in flowing fluids. Often these particles are used as passive tracers, with the sole purpose of making the fluid motions visible or measurable. In certain cases, however, the particle motions do not merely follow the fluid flow, and become of interest in their own right. For buoyant bubbles or massive grains, autonomous motions may result from density differences with respect to the surrounding fluid. At high particle concentrations, the particles may also exert influence on each other. Even when they are neutrally buoyant and sparsely distributed, rigid particles may actively interact with the fluid as a result of finite size effects.

An intriguing example of such finite size effects is provided by shear induced migration in non-homogeneous laminar shear flows. The simplest case is the case of Poiseuille flow, sparsely seeded with neutrally buoyant solid particles of finite size. Experimental observations show that the particles do not distribute themselves evenly over the cross-section of the circular pipe, but instead migrate towards ring-shaped regions of preferential concentration. The radial symmetry in that case facilitates both observations and analysis, hence Poiseuille flow has been the focus of most studies to date (Segré and Silberberg 1962; Matas et al. 2004).

It is currently unclear how such size effects play out in flows exhibiting a fully three-dimensional internal structure, and this constitutes the concern of the present work. The flow configuration chosen is the lid-driven cubic cavity. This is a closed system, with a well-defined geometry and boundary motion. Liquid is enclosed between five rigid walls, and driven by a top lid moving at constant speed. Despite its simplicity, the configuration

generates complex flows, featuring three-dimensional circulation and a rich vortex structure.

This flow structure is now well-documented thanks to a number of computational and experimental studies. In three dimensions, computational solutions have been obtained both for Stokes flow (Murugesan et al. 2005), corresponding to vanishing Reynolds numbers, and for the full Navier-Stokes equations at Reynolds numbers up to $Re = 2000$ (Chiang et al. 1997, 1998; Lo et al. 2005). In the laboratory, both dyes and passive tracer particles have been used to visualise and measure the flow field inside lid-driven cavities (Pan and Acrivos 1967; Koseff and Street 1984; Guermond et al. 2002; Migeon 2002). In most of these experiments, laser light sheets were used to highlight motions within 2D slices of the 3D flow. An overall review of the fluid mechanics of driven cavities is provided by Shankar and Deshpande (2000).

Rather than the fluid flow field, the present work focuses on the motions of suspended particles inside the cavity. Instead of a large number of minute passive tracers, the flow is seeded with a small number of neutrally buoyant solid particles of finite size. Our aim is to capture the long time trajectories of these particles, as they transit along orbits embedded within the three-dimensional liquid flow. The corresponding experimental requirements are rather different from those faced by the aforementioned researchers. First, interest is focused here on continuous Lagrangian trajectories rather than local velocities of the Eulerian flow field. Secondly, the particle paths are three-dimensional, and full volume imaging must be preferred over the plane slices resulting from laser light sheet illumination. Finally, the ultimate objective of the work is to highlight effects associated with particle migration. Since these effects are expected to be small, careful attention must be devoted to estimating and reducing experimental errors.

The following combination of techniques is adopted to meet these requirements. Particle Tracking Velocimetry (PTV) is chosen to continuously track individual particles along their paths. Stereoscopic imaging is selected to pinpoint the three-dimensional positions of particles along these trajectories. By using small numbers of back-illuminated particles, clear particle images can be seen on two distinct viewpoints without risk of occlusion. Finally, error control is pursued through two means. Pixel errors in the image plane are projected into the 3D viewing volume to estimate raw positioning errors. Along their trajectories, the position histories of individual particles are then treated as noisy stochastic data that can be systematically filtered using Kalman filter.

This approach brings together tools from two different origins. Particle Tracking Velocimetry is now a well-established technique of experimental fluid mechanics (for a review, see Adrian, 1991). While not yet as mature as their 2D counterparts, 3D PTV techniques have been documented in a number of recent works (Maas et al. 1993; Ushijima et al. 1996; Virant and Dracos 1997; Kieft et al. 2002). The stereoscopic PTV technique implemented in the present work builds on earlier work by Spinewine *et al.* (2003) and Douchamps *et al.* (in press). Beyond experimental fluid mechanics, the target tracking problem has been the focus of much applied work in signal treatment (Shah et al. 1993; Castellari et al. 2001; Ito et al. 2001; Liao 2002). Much of this work is centred on applications of the Kalman filter (Kalman, 1960), used in the present work to attenuate the effect of measurement errors. For 2D PTV, Kalman filter was used for a similar purpose by Hu (2003).

The present paper is structured as follows. In the following section, the laboratory setup used to conduct the lid-driven cavity flow experiments is first presented. Next, the methods used to position particles in the 2D image plane and inside the 3D viewing volume are documented, along with corresponding error estimates. The Kalman filter approach used to reduce the

effect of positioning errors on the particle trajectories is then detailed. Finally, measurements of the trajectories of suspended particles in the lid-driven cavity are described, followed by the overall conclusions of the work.

2

Experimental setup

Experiments are performed using the apparatus shown on Figure 1. The phenomena of interest occur in a small cubic cavity having side $S = 10$ cm, filled with liquid, in which a small number of neutrally buoyant solid spheres are suspended. This inner cavity has transparent rigid walls on five sides, and a moving lid on the top side. The moving lid is obtained by placing on the open top face of the cavity an upside down conveyor belt system, driven by a variable speed motor. The inner cavity is itself placed inside a larger plane-walled enclosure. This outer tank is filled with liquid up to a level slightly above the conveyor belt lid. In this way, the lubrication flow that inevitably occurs through the small gaps between the conveyor belt and the top of the cavity side walls does not lead to liquid loss from the cavity.

The liquid used for the experiments is a mixture of water and glycerin. The properties of the mixture are: kinematic viscosity $\nu = 37.2$ mm²/s and specific gravity S.G. = 1.21. The suspended solid particles have a diameter of 3 mm and the same specific gravity as the liquid. The particles are coloured dark blue and are found easiest to image using back-illumination. Their motions are filmed under two different viewpoints, respectively through the back wall and the side wall of the inner cavity. This is done using a single camera supplemented by a system of mirrors. The imaging sensor used is a TRV950 Sony DV camera operating in interlaced mode at a frequency of 30 Hz. Images have a resolution of 480×640 pixels.

The camera selected allows compression-free acquisition of digital images over long durations. This permits continuous taping of each experiment, spanning both the sudden start-up of the conveyor belt and the long time regime established after many cycles. Lines of known interdistance are marked on the conveyor belt, allowing the belt speed to be monitored as well on the video. The test case used below to illustrate the methods was obtained at belt speed $V = 17.5$ cm/s, corresponding to a Reynolds number $Re = VS/\nu = 470$. The total recording duration for this run was 7 minutes. Further details of the lid-driven cavity device and imaging configuration are illustrated on Fig. 1.

3

Particle positioning

3.1

Particle positioning on the 2D images

The image analysis is performed entirely off-line. Once retrieved, the digital images are de-interlaced. This yields images of twice the frequency (60 Hz instead of 30 Hz), but half the vertical resolution (240 instead of 480 pixels). Image treatment then proceeds in the following steps. First, the gray scale is inverted to transform the back-illuminated dark particles into bright spots over a dark backdrop. Next, a background image is obtained by averaging over the full image sequence. Difference images are then obtained by subtracting the background from each frame. This makes it easier to distinguish moving particles from static features of the images.

Standard methods are used to locate particles on these different images. Each image frame is

first convoluted with a Laplacian-of-Gaussian mask to highlight the bright particles of known pixel size. Local brightness maxima with peak values beyond a certain threshold are selected as particle centroids, and their positions are refined to subpixel accuracy using a quadratic fit. For more details, the reader is referred to Capart *et al.* (2002).

To make these procedures more robust, dynamic thresholding is used in the present work. Instead of choosing a constant threshold for particle identification, the threshold is set anew for each frame based on the previously observed brightness maxima. Typically the threshold is scaled down to $2/3$ of the brightness maximum of the least conspicuous particle on the previous frame. This makes it easier to track particles over long time, during which they may gradually transit through regions of uneven illumination.

Results obtained using the above methods are illustrated on Fig. 2. Each panel shows a stereo view of the trajectories of two suspended solid particles, with the front view on the left and the side view on the right. For comparison purposes, panel 2a shows an artificial long exposure image, obtained simply by recording the brightest pixel of a sequence at each position. This highlights trajectories without recourse to any image analysis. For the same sequence, panel 2b shows the marked particle positions acquired using the above algorithms. Overall, good results are obtained. A small proportion of wrongly positioned particles is nevertheless present, and will have to be dealt with at later stages of the analysis.

3.2

Three-dimensional stereo positioning

Once particles have been positioned on images from both viewpoints, their positions in 3D space can be found by locating the intersections of stereoscopic rays. As illustrated on Fig. 3, rays associated with two different viewpoints can be written in the parametric form

$$\mathbf{x}(\lambda) = \mathbf{p} + \lambda \mathbf{q}, \quad \mathbf{x}'(\lambda') = \mathbf{p}' + \lambda' \mathbf{q}', \quad (1,2)$$

where vector $\mathbf{x} = (x, y, z) = (x_1, x_2, x_3)$ denotes a position in 3D space, vector $\mathbf{p} = (p_1, p_2, p_3)$ denotes the 3D position of the projection centre of the first viewpoint, vector $\mathbf{q} = (q_1, q_2, q_3)$ gives the ray direction, and scalar λ is the free parameter. The same symbols marked with a prime denote corresponding entities for the second viewpoint.

The free parameters λ and λ' are due to the depth ambiguity associated with 2D images: in the absence of other information, the location of a particle along a given ray is not known. This ambiguity must be resolved by using information from two different viewpoints. Provided rays from two such viewpoints are associated with one and the same physical particle, the 3D position of the particle will lie at the intersection of the rays. In practice, accuracy limitations prevent rays from perfectly intersecting each other. Instead, one seeks an approximate intersection point, defined as the midpoint of the shortest line segment linking the two rays (see Fig. 3). The parameters λ , λ' specifying the endpoints of this segment on each ray are the solutions of the linear system

$$\begin{pmatrix} \mathbf{q}^T \mathbf{q} & -\mathbf{q}^T \mathbf{q}' \\ \mathbf{q}'^T \mathbf{q} & -\mathbf{q}'^T \mathbf{q}' \end{pmatrix} \begin{pmatrix} \lambda \\ \lambda' \end{pmatrix} = \begin{pmatrix} \mathbf{q}^T (\mathbf{p}' - \mathbf{p}) \\ \mathbf{q}'^T (\mathbf{p}' - \mathbf{p}) \end{pmatrix}, \quad (3)$$

which states that the shortest line segment must be perpendicular to both rays. In this equation as well as other equations below, vectors are taken as column arrays and superscript T denotes the transpose. The midpoint position and distance of closest encounter are then given by

$$\mathbf{y} = \frac{1}{2} \{ \mathbf{x}(\lambda) + \mathbf{x}'(\lambda') \}, \quad e = \| \mathbf{x}'(\lambda') - \mathbf{x}(\lambda) \|. \quad (4,5)$$

Position \mathbf{y} provides an approximation of the true position of the particle, while the distance e provides an indication of the closeness of the intersection. When many particles are present, pairs of rays from the two viewpoints are selected by minimising the sum of their inter-ray distances, using the methods detailed in Spinewine *et al.* (2003). Once ray pairs have been

obtained, their inter-ray distances also provide a measure of the accuracy of the stereoscopic reconstruction. This will be exploited below to estimate particle positioning errors.

3.3

Camera calibration

The parametric ray equations (1) and (2) are related as follows to the pixel coordinates of particles in each image plane. The image formation process is modelled as a perspective projection. As illustrated on Fig. 3, direction vector \mathbf{q} can then be decomposed as the sum

$$\mathbf{q} = \mathbf{d} + \gamma \mathbf{c} + \rho \mathbf{r}, \quad (6)$$

where (γ, ρ) are the (column, row) pixel coordinates of the particle centroid, depth vector \mathbf{d} denotes the position of the origin of the image plane relative to the projection centre \mathbf{p} , and vectors \mathbf{c} and \mathbf{r} are direction vectors of the image plane, associated respectively with column and row directions of the digital images. Equation (6) can be read as a parametric plane equation in which the two free parameters are the pixel coordinates (γ, ρ) . The parametric ray equation (1) can then be rewritten in the matrix form

$$\mathbf{x}(\lambda) = \mathbf{p} + \lambda \begin{pmatrix} | & | & | \\ \mathbf{c} & \mathbf{r} & \mathbf{d} \\ | & | & | \end{pmatrix} \begin{pmatrix} \gamma \\ \rho \\ 1 \end{pmatrix} = \mathbf{p} + \lambda \mathbf{S} \begin{pmatrix} \gamma \\ \rho \\ 1 \end{pmatrix} \quad (7)$$

where the screen matrix \mathbf{S} has vectors \mathbf{c} , \mathbf{r} , \mathbf{d} as columns. Provided that projection centre \mathbf{p} and screen matrix \mathbf{S} are known, relation (7) transforms pixel coordinates on a 2D image into a parametric ray equation in 3D space. By marking each symbol with a prime, similar equations can of course be written for the second viewpoint.

The issue that remains to be addressed is the problem of estimating parameters \mathbf{p} , \mathbf{S} and \mathbf{p}' , \mathbf{S}' for the two viewpoints. This is the camera calibration problem, which can be solved by first acquiring images of calibration markers of known positions placed in the viewing

volume of interest. The knowledge of at least 6 points of known image (2D) and world (3D) coordinates is sufficient to obtain the 3 components of vector \mathbf{p} and the 9 components of matrix \mathbf{S} . For this purpose, relation (7) is first inverted to obtain

$$\lambda \begin{pmatrix} \gamma \\ \rho \\ 1 \end{pmatrix} = \mathbf{A} \begin{pmatrix} x \\ y \\ z \end{pmatrix} + \mathbf{b} \quad (8)$$

where $\mathbf{A} = \mathbf{S}^{-1}$ and $\mathbf{b} = -\mathbf{S}^{-1}\mathbf{p}$. This relation can be observed to be linear in all the unknowns λ , a_{ij} , and b_j . A stacked system of linear equations can thus be assembled with coefficients given by the known 2D and 3D coordinates (γ, ρ, x, y, z) of each calibration point. A minor complication is that the resulting system is homogeneous and admits a trivial solution in which all unknowns are zero. This hurdle is easy to overcome by setting one the unknowns equal to an arbitrary non-zero value. For 6 or more calibration points, the system is over-determined and can be solved by linear least squares. The coefficients of \mathbf{p} and \mathbf{S} can finally be obtained from the coefficients of \mathbf{A} and \mathbf{b} using straightforward linear algebra. In practice, it is advised to choose more than 6 points, well-distributed in the viewing volume of interest. In the present experiments, 12 points are used: the 8 corners of the cubic inner cavity supplemented by 4 points in a diagonal plane. For stereo imaging, the procedure must of course be applied to both viewpoints. More details about camera calibration can be found in Spinewine *et al.* (2003).

Once the two viewpoints have been calibrated, stereo rays can be used to find 3D particle positions using the method of section 3.2. Figure 4 shows the corresponding results for the particles depicted earlier in Fig. 2. Qualitatively, the observed 3D trajectories are consistent with the information that can be visually inferred from the 2D views of Fig. 2. To assess the results quantitatively as well, positioning errors associated with the stereo procedure are examined in the next section.

3.4

Error estimation

The errors incurred by the above procedure can be split in two classes: 1) a small proportion of misidentified particles, and 2) measurement inaccuracies affecting correctly identified particles. Particles can be misidentified at both the 2D and 3D stages: spurious features can be wrongly identified as particles on the 2D images (see Fig. 2), or stereo mismatches can occur when more than one particle is present in the viewing volume.

In the present work, the number of such mistakes is kept relatively low (compared for instance with the work reported by Spinewine et al. 2003 and Douxchamps et al, in press), thanks to two features of the present experiments. First, motions are observed in a cavity with five transparent sides, allowing good control of the illumination conditions. Secondly, experiments are performed with only a limited number of particles, going from one to a maximum of 10 particles. To screen out misidentified particles from the data set, a simple outlier filtering procedure is used. For a given particle, positions which exceed a moving average position by more than 4 times a median absolute deviation are excluded from the set. Outliers screened out in this way are circled on Fig. 5. For the present experiment, this leads to the exclusion of less than 3 % of the data.

On the other hand, the random position errors affecting correctly identified particles are estimated as follows. In the present experiments, the optical axes of the two viewpoints are nearly orthogonal to each other and lie in a horizontal plane. This means that 3D position errors are simple to relate to 2D positioning errors on the digital images. Due to de-interlacing, the pixel resolution in the vertical (row) direction is half the resolution in the horizontal

direction (column). Root-mean-squared (rms) position errors in the row and column directions are thus expected to follow the ratio

$$\varepsilon_r = 2\varepsilon_c, \quad (9)$$

where both are expressed in column pixel units. The corresponding position errors in 3D space are given by

$$\varepsilon_x = \varepsilon_y = \alpha\varepsilon_c, \quad \varepsilon_z = \frac{\alpha}{\sqrt{2}}\varepsilon_r, \quad (10)$$

where α is a scale factor and the $\sqrt{2}$ denominator is an error attenuation produced by the average used to estimate midpoint (4), under the assumption that random position errors are identically distributed and uncorrelated. This error attenuation is only operative in the z -direction, which corresponds to the row direction of both viewpoints. Likewise, the inter-ray distance (5) is related to the row error through

$$e = \alpha\sqrt{2}\varepsilon_r. \quad (11)$$

Both the scale factor α and inter-ray distance e can be measured in the experiments. Based on the calibrated viewpoints, the scale factor is approximately $\alpha \approx 0.3$ mm/(column pixel). Using the full set of ray pairs acquired in a typical experiment, on the other hand, the rms inter-ray distance is of the order of $e = 0.6$ mm. Using (9), (10) and (11), rms errors for the raw stereo measurements of the 3D particle positions are found to be of the order of

$$\varepsilon_x = \varepsilon_y = 0.2 \text{ mm}, \quad \varepsilon_z = 0.3 \text{ mm}, \quad (12)$$

and a combined position error can be obtained from

$$\varepsilon = \sqrt{\varepsilon_x^2 + \varepsilon_y^2 + \varepsilon_z^2} = 0.4 \text{ mm}. \quad (13)$$

The corresponding root-mean-squared pixel error is $\varepsilon_c = 0.7$ pixel. This is slightly higher than typical errors reported in 2D PTV experiments (Veber et al. 1997; Capart et al. 2002). Note however that the error estimate obtained here includes both 2D image positioning errors and 3D geometrical effects (limited accuracy of the camera calibration and possible

departures from the assumed perspective projection). As explained in the next section, the error level can be reduced further by applying Kalman filters to the particle trajectories.

4

Kalman filtering of the particle trajectories

4.1

Measurement and signal models

The stereo methods described above yield sets of 3D particle positions extracted from sequences of images. Long time trajectories are then constructed by linking together successive particle positions. When more than one particle is present in the cavity, a criterion must be invoked to decide which particle at one instant corresponds to which particle at the next instant. Since the present experiments involve small numbers of particles (maximum 10) embedded in a relatively regular flow, this particle tracking task is not difficult to carry out. A simple nearest-neighbour scheme (see e.g. Guler et al. 1999) is used, subject to the condition that a particle can participate in only one trajectory (see Capart et al. 2002). The trajectory of each particle yields Lagrangian time series of raw position measurements. Such time series are shown on Fig. 5 for the three evolving spatial coordinates of a single particle.

To fill in data gaps and attenuate the effect of measurement noise, Kalman filtering can now be applied to the three-dimensional position history of a given particle. The approach is based on an idealised model of the measurement and physical processes. The measurement model is simply

$$\mathbf{y}_k = \mathbf{x}_k + \mathbf{m}_k \quad (14)$$

where vector \mathbf{x}_k denotes the true 3D particle position $(x_1(t_k), x_2(t_k), x_3(t_k))$ at time t_k ,

vector \mathbf{y}_k denotes the measured particle position at the same instant, and \mathbf{m}_k represents the corresponding measurement noise. On the other hand, the physical particle trajectory is assumed to be governed by the following discrete signal model:

$$\begin{pmatrix} \mathbf{x}_k \\ \mathbf{u}_k \end{pmatrix} = \mathbf{F} \begin{pmatrix} \mathbf{x}_{k-1} \\ \mathbf{u}_{k-1} \end{pmatrix} + \begin{pmatrix} \mathbf{0} \\ \mathbf{n}_{k-1} \end{pmatrix} \quad (15)$$

where vector \mathbf{u}_{k-1} denotes the particle velocity averaged from time t_{k-1} to time t_k . In the above equation, the matrix \mathbf{F} is given by

$$\mathbf{F} = \begin{pmatrix} \mathbf{I} & \Delta t \mathbf{I} \\ \mathbf{0} & \mathbf{I} \end{pmatrix} \quad (16)$$

where \mathbf{I} is the 3×3 identity matrix and $\Delta t = t_k - t_{k-1}$ is the time interval between successive observations. Matrix \mathbf{F} represents the kinematic relation linking two successive states $(\mathbf{x}_{k-1}; \mathbf{u}_{k-1})$ and $(\mathbf{x}_k; \mathbf{u}_k)$. This deterministic link is perturbed by adding to the velocity vector \mathbf{u} a random signal noise \mathbf{n} .

The signal noise contribution accounts for the uncertain physical dynamics that lead to particle accelerations. It is conceptually distinct from the measurement noise \mathbf{m} introduced earlier. The two noise contributions nevertheless share one simplifying feature: the components of both vectors \mathbf{m}_k and \mathbf{n}_k at each time index k are assumed to be uncorrelated, normally distributed random variables of zero mean. Note that because the signal noise enters through the velocities, the physical position variations retain some correlation in time.

Upon defining the full state vector

$$\mathbf{z} = \begin{pmatrix} \mathbf{x} \\ \mathbf{u} \end{pmatrix}, \quad (17)$$

relations (14) and (15) can be rewritten more compactly as

$$\mathbf{y}_k = \mathbf{H} \mathbf{z}_k + \mathbf{m}_k, \quad \mathbf{z}_k = \mathbf{F} \mathbf{z}_{k-1} + \mathbf{n}_{k-1} \quad (18, 19)$$

where $\mathbf{H} = (\mathbf{I} \mid \mathbf{0})$. Vectors \mathbf{n}_{k-1} now feature 6 components instead of 3, but it is implied that the first three components are zero. The equations are now in standard form, facilitating application of the Kalman filter.

4.2

Forward Kalman filter

An optimal filtered estimate $\tilde{\mathbf{x}}_k$ of the particle position history can now be obtained using the well-known Kalman filter (Kalman and Bucy 1960; Brown and Huang 1997; Welch and Bishop 2001). The filter proceeds recursively, through repeated application of two successive steps: a time update and a measurement update. First, a time update is performed using

$$\hat{\mathbf{z}}_k = \mathbf{F} \tilde{\mathbf{z}}_{k-1}. \quad (20)$$

This first step uses deterministic matrix \mathbf{F} to predict the state at the next time instant based on the previous filtered state $\tilde{\mathbf{z}}_{k-1}$. If measurement \mathbf{y}_k is not available, the predicted state $\hat{\mathbf{z}}_k$ is adopted without correction. Although such data gaps are relatively rare, they occur whenever a particle position has been missed (typically due to occlusion effects if many particles are present) or when a particle position has been rejected as an outlier. Most often a valid measurement \mathbf{y}_k is available, and the second step is a measurement update written

$$\tilde{\mathbf{z}}_k = \hat{\mathbf{z}}_k + \mathbf{K}_k (\mathbf{y}_k - \mathbf{H} \hat{\mathbf{z}}_k) \quad (21)$$

where \mathbf{K}_k is the Kalman gain matrix. In this second step, the new filtered state is estimated by making a correction proportional to the discrepancy between the predicted state and the actual measurement \mathbf{y}_k . The weight given to the measurement relative to the prediction is governed by the Kalman gain matrix \mathbf{K}_k . This matrix is constructed to minimize the a posteriori error covariance

$$\tilde{\mathbf{P}}_k = E[(\tilde{\mathbf{z}}_k - \mathbf{z}_k)(\tilde{\mathbf{z}}_k - \mathbf{z}_k)^T]. \quad (22)$$

The Kalman matrix and error covariance matrix are themselves obtained through a recursive

process composed of three successive steps:

$$\hat{\mathbf{P}}_k = \mathbf{F} \tilde{\mathbf{P}}_{k-1} \mathbf{F}^T + \mathbf{Q}, \quad (23)$$

$$\mathbf{K}_k = \hat{\mathbf{P}}_k \mathbf{H}^T (\mathbf{H} \hat{\mathbf{P}}_k \mathbf{H}^T + \mathbf{R})^{-1}, \quad (24)$$

$$\tilde{\mathbf{P}}_k = (\mathbf{I} - \mathbf{K}_k \mathbf{H}) \hat{\mathbf{P}}_k, \quad (25)$$

where matrices \mathbf{R} and \mathbf{Q} are the covariances of the measurement noise and physical noise, respectively. They are given by

$$\mathbf{R} = E[\mathbf{m}_k \mathbf{m}_k^T] = \begin{pmatrix} \varepsilon_1^2 & 0 & 0 \\ 0 & \varepsilon_2^2 & 0 \\ 0 & 0 & \varepsilon_3^2 \end{pmatrix}, \quad \mathbf{Q} = E[\mathbf{n}_k \mathbf{n}_k^T] = \begin{pmatrix} \mathbf{0} & | & \mathbf{0} \\ \mathbf{0} & | & \sigma^2 \mathbf{I} \end{pmatrix}. \quad (26)$$

For the measurement noise, the variances ε_1^2 , ε_2^2 and ε_3^2 characterising position errors in the three space directions were obtained earlier from an analysis of the stereo imaging procedure (see eq. 12). On the other hand, the variance σ^2 of the physical signal noise is unknown a priori. In the absence of more information, it is assumed to be the same for all three velocity components.

4.3

Forward-backward Kalman filter

In practice, results obtained with the above forward filtering pass are not entirely satisfactory. In addition to attenuating high-frequency noise, which is the desired outcome, the filter shifts the signal in time. As illustrated on Fig. 6, this effect is especially pronounced when a low signal variance σ^2 is assumed. A remedy is to apply both a forward and a backward pass to the signal and to blend their results (see Brown and Huang 1997). In this case, let $\tilde{\mathbf{z}}_{k-1}$ denote the filtered state at time t_{k-1} obtained by starting from t_1 and applying the Kalman filter forward in time. Matrix $\tilde{\mathbf{P}}_{k-1}$ denotes the corresponding error covariance. Steps (21)

and (23) can then be used to perform the time updates,

$$\hat{\mathbf{z}}_k = \mathbf{F} \tilde{\mathbf{z}}_{k-1} \quad \text{and} \quad \hat{\mathbf{P}}_k = \mathbf{F} \tilde{\mathbf{P}}_{k-1} \mathbf{F}^T + \mathbf{Q} \quad (27,28)$$

where hats indicate quantities obtained by forward prediction. If n successive position measurements are available, a filtered state $\bar{\mathbf{z}}_k$ and error covariance $\bar{\mathbf{P}}_k$ at time t_k can likewise be obtained by starting from t_n and applying the Kalman filter backward in time. A blended estimate can then be obtained from the weighted sum

$$\bar{\mathbf{z}}_k = (\hat{\mathbf{P}}_k^{-1} + \bar{\mathbf{P}}_k^{-1})^{-1} (\hat{\mathbf{P}}_k^{-1} \hat{\mathbf{z}}_k + \bar{\mathbf{P}}_k^{-1} \bar{\mathbf{z}}_k), \quad (29)$$

which constitutes the result of the forward-backward filter. Note that by using time updates (27) and (28), the forward pass does not make use of measurement \mathbf{y}_k , which is used only by the backward pass. This is needed to avoid using the same information twice. Results obtained with this forward-backward version of the Kalman filter are also shown on Fig. 6. It is seen that the time shift has vanished, leaving only the desired signal attenuation.

4.4

Filter tuning

The degree of attenuation produced by the filter is governed by the relative strength of the measurement error and physical noise, gauged by non-dimensional ratio $\beta = \sigma \Delta t / \varepsilon$. This ratio depends both on the known measurement error level ε and on the unknown physical noise strength σ . The last issue to be addressed is therefore the choice of physical noise strength σ , or equivalently the choice of ratio β used to tune the filter. As illustrated on Fig. 7, different values of β lead to contrasted outcomes. High values of β imply that the observed random jitter of the signal is mainly physical in origin, and should not be attenuated. On the other hand, low values imply that most of the jitter is due to measurement noise, and should be filtered out. The Kalman filter responds accordingly, attenuating the signal in

inverse proportion to ratio β .

Since the true physical signal is unknown, it is a priori unclear how β should be chosen. The approach adopted is to apply the forward-backward filter to the signal for various values of ratio β , and to monitor the mean-squared difference between the resulting filtered positions $\bar{\mathbf{x}}_k(\beta)$ and the raw measured positions \mathbf{y}_k . In contrast with the random measurement noise, the physical position jitter is expected to be correlated in time. It is thus less sensitive to attenuation and we can assume that for the correct choice of β , the filtered positions $\bar{\mathbf{x}}_k(\beta)$ provide a reasonable approximation of the true signal \mathbf{x}_k . The mean-squared difference between $\bar{\mathbf{x}}_k(\beta)$ and \mathbf{y}_k should then be close to the known measurement noise variance ε^2 . This motivates the following rule of thumb: our choice for β is the value which yields a mean-squared difference between $\bar{\mathbf{x}}_k(\beta)$ and \mathbf{y}_k equal to the known error variance ε^2 . The criterion is illustrated on Fig. 8, and the resulting filtered signal is plotted as a thick line on Fig. 7. Although a more rigorous criterion would be highly desirable, the rule of thumb adopted appears to yield visually plausible results.

5

Results and discussion

5.1

Time series of particle positions

Time series of the three components of the filtered position $\bar{\mathbf{x}}$ of a single particle (noted x, y, z for simplicity in the legend) are plotted on Fig. 9. Here the first 3 minutes of an overall measured span of 7 minutes are represented. Beyond the first minute, the observed

motions stay similar in character for the rest of the sequence, indicating that an asymptotic stationary regime has been reached. Various features of the particle orbits can be observed on these plots.

Overall, the particle motions feature two main components: fast laps in the x - z plane and slow sideways motions in the y -direction. First, the x - and z - position histories exhibit fast oscillations of gradually varying amplitude and period, out-of-phase with each other by 90 degrees. This implies spiral motions of the particle about a rotation axis parallel to the y -direction. These motions directly reflect the rotational flow induced by the longitudinally driven lid. The outermost excursions of the particle bring it close to the conveyor belt, located at plane $z = 10$ cm. As the particle approaches the upstream edge of the belt (line $x = 0$, $z = 10$ cm), it makes a characteristic hairpin turn. Upon reaching the downstream edge (line $x = 10$ cm, $z = 10$ cm), it makes a sharp downward turn where accelerations greater than anywhere else along the cycle are observed.

In addition to these fast laps around the cavity, the y -position history exhibits slow cycles of lateral motion. Rather than staying within a single plane, the particle swerves sideways. These slow lateral motions have large amplitudes, bringing the particle very near the centre plane ($y = 5$ cm) and the right lateral wall of the cavity ($y = 0$ cm). Similar motions (not shown) are observed for a second particle located to the left of the centre plane. At this Reynolds number, particles are not observed to ever cross the centre plane of the cavity. Comparing the different time histories with each other, it is clear that the evolution of the amplitude of the rapid x - z cycles is modulated by the slow lateral motions. This modulation is not quite periodic. Instead, irregular cycles of variable duration are observed throughout the sequence. Nevertheless, a generic feature of these cycles is that the particle lingers near the centre plane, but makes only short-lived excursions to the neighbourhood of the sidewall. Other features of the particle

trajectory are easier to understand based on 3D views, and are discussed in the next subsection.

5.2

Three-dimensional trajectory of an individual particle

For clarity, it is convenient to look separately at two shorter segments of the orbits, shaded in grey on Fig. 9: the start-up phase, immediately following the sudden start of the conveyor belt, and a typical cycle of the asymptotic regime. Three-dimensional views of the corresponding trajectories are plotted on Figures 10 and 11, respectively.

At the beginning of the start-up phase, the particle is located near the centre plane and along the top lid. This position is marked as a black dot on the 4 panels of Fig. 10. After the sudden start of the conveyor belt, the particle is entrained into circular orbits. At first, the orbit is tightly wound and confined to the downstream end of the cavity, but then gradually spirals outwards. Throughout these expanding orbits, the particle stays near the centre plane. Upon reaching the perimeter of the cavity, the orbit finally exhibits its first significant lateral drift, moving outwards towards the side wall (plane $y=0$) along the back face (plane $x=0$). This orbit corresponds to a transient phase of the liquid flow field.

A more complete orbital cycle is shown on Fig. 11. The cycle corresponds to a later time, after establishment of an asymptotic regime of qualitatively recurrent behaviour. The specific cycle chosen, somewhat longer than typical cycles, was selected because it shows the orbital pattern particularly clearly. Starting from a position near the side wall of the cavity, the particle spirals inwards toward the centre plane. The spiral is at first tightly wound, but gradually expands as the centre plane is approached. Compared to the start-up phase, the axis of the spiral is closer to the centroid of the cavity, but remains in the upper downstream quadrant.

Near the centre plane, the particle makes a few more laps, while continuing to slowly spiral outwards toward the perimeter of the cavity. Finally the particle drifts back toward the side wall along the back and bottom faces of the cavity (planes $x = 0$ and $z = 0$, respectively).

5.3

Trajectories of 10 orbiting particles

The experimental run examined until now was a run conducted with 2 particles only, and attention was focused on the motions of a single one of them. To demonstrate the wider applicability of the technique and highlight certain additional features, this last subsection presents results for a run involving 10 simultaneously orbiting particles. The corresponding Reynolds number is slightly higher at $Re = VS/\nu = 1030$. All 10 particles were initially placed in the right half of the cavity, and stayed there for the entire run. Other runs conducted with particles on both sides showed a high degree of symmetry.

Figure 12 shows the orbits of the 10 particles, as tracked over 500 successive frames (a segment of 17 seconds in the asymptotic regime after the start-up transient has died out). Panel a of Fig. 12 shows a stereoscopic long exposure image, while panels b to d show the corresponding 3D trajectories. Like the image of Fig. 2a, the long exposure view of Fig. 12a is produced directly from the video frames and does not rely on the positioning algorithms. By contrast, the curves plotted on panels b to d represent stereo measurements, after full processing by the forward-backward Kalman filters. The juxtaposition of these two independently produced results can be used as a qualitative check of the methods. Encouragingly, jitter due to measurement noise is attenuated by the Kalman filters, without significantly distorting the shapes of the orbits. Less systematic filtering procedures tried in the initial stages of the present work, by contrast, produced unacceptable distortion.

The results also highlight the most intriguing feature of the experiments. Despite starting from arbitrary positions and being allowed to wander freely within the cavity, the neutrally buoyant particles do not explore all regions of the flow. Instead, they tend to cluster along preferential pathways of the internal circulation: an inner coil along which particles spiral inwards from the sidewall toward the centre plane, and an outer coil along which particles drift back from the centre plane toward the sidewall. Conversely, there are various zones in which the particles do not venture: 1) the core of the main vortex, near the centre of the cavity, 2) the corner eddies located at the four corners of the bottom face of the cavity; 3) a toroidal zone located between the inner and outer coils along which particles spiral inward and outward. While the origin of these preferential pathways requires further scrutiny, we interpret them as resulting from particle migrations toward certain belt zones of the flow. Assuming that the underlying mechanism is similar to the one observed in Poiseuille flows, these migrations would be due to the finite size of the solid particles relative to the local variations in the liquid shear.

6

Conclusions

In the present work, stereo imaging and signal processing techniques were combined to monitor the three-dimensional orbits of individual particles in a lid-driven cavity flow. Using a digital camera, video sequences of long duration were acquired, continuously recording the particle motions under two different viewpoints. By tracing calibrated rays into the viewing volume, the 3D particle positions and corresponding measurement errors were estimated. To attenuate the effect of these errors, the position signals were then processed by Kalman filters, based on a simple stochastic model of the kinematics. Kalman filters with forward and

backward passes were found to give good results, attenuating the noise without shifting the signals in time or significantly distorting the orbital shapes.

The measured particle trajectories present a number of interesting characteristics. Overall, the particles are observed to undergo spiral motions modulated by sideways excursions from the centre plane to the side wall and back. These spiral motions are found to exhibit slightly different patterns during the start-up phase and the subsequent regime. Observed over long times, particle trajectories are seen to cluster along certain pathways of the internal circulation, and avoid altogether certain regions of the cavity flow. Such preferential migrations appear due to finite size effects, similar to those observed for neutrally buoyant solid particles in laminar Poiseuille flows. Here however the viscous flow in which the particle motions are embedded features a more complicated, fully three-dimensional internal structure.

The research suggests various avenues for further work. The measurement methods could benefit from a number of improvements. Instead of using the Kalman filters at the post-processing stage only, they could be incorporated already at the particle tracking stage. This could make the methods more robust, allowing them to deal with more difficult illumination conditions or larger numbers of simultaneously orbiting particles. More rigorous ways of tuning Kalman filters would also be desirable. On the other hand, further work is needed to enhance our understanding of the motions of solid particles suspended in three-dimensional viscous flows. For the lid-driven cavity, we are currently engaged in efforts aimed to characterise particle trajectories over a wider range of Reynolds numbers, and to probe the relationship between the Lagrangian particle trajectories and the Eulerian viscous flow field.

References

- Adrian RJ** (1991) Particle-imaging techniques for experimental fluid mechanics. *Annu Rev Fluid Mech* 23: 261-304.
- Brown RG; Hwang PYC** (1997) Introduction to random signals and applied Kalman filtering. Wiley, New York.
- Capart H; Young DL; Zech Y** (2002) Voronoï imaging methods for the measurement of granular flows. *Exp Fluids* 32: 121-135.
- Castellari S; Griffa A; Özgökmen TM; Poulain PM** (2001) Prediction of particle trajectories in Adriatic Sea using Lagrangian data assimilation. *J Mar Syst* 29: 33-50.
- Chiang TP; Hwang RR and Sheu WH** (1997) On end-wall corner vortices in a lid-driven cavity. *J Fluids Eng* 119: 201-106.
- Chiang TP; Sheu WH; Hwang RR** (1998) Effect of Reynolds number on the eddy structure in a lid-driven cavity. *Int J Numer Meth Fluids* 26: 577-579.
- Douxchamps D ; Devriendt D; Capart H ; Craeye C ; Macq B ; Zech Y** (in press) Stereoscopic and velocimetric reconstructions of the free surface topography of antidune flows. *Exp Fluids*, in press.
- Guermond JL; Migeon C; Pineau G; Quartapelle L** (2002) Start-up flows in a three-dimensional rectangular driven cavity of aspect ratio 1:1:2 at $Re = 1000$. *J Fluid Mech* 450: 169-199.
- Guler M; Edil TB; Bosscher PJ** (1999) Measurement of particle movement in granular soil using image analysis. *J Comp Civ Eng* 13:116-122.
- Hu CC** (2003) Analysis of motility for aquatic sperm in videomicroscopy. MSc thesis, Department of Bio-Industrial Mechatronics Engineering, National Taiwan University.
- Ito M; Tsujimichi S; Kosuge Y** (2001) Tracking a three-dimensional moving target with distributed passive sensors using extended Kalman filter. *Electron Commu Japan Part 1* 84(7): 74-85.

- Kalman RE** (1960) A new approach to linear filtering and prediction problem. *J Basic Eng* ASME , 35-45.
- Kieft RN; Schreel K; van der Plas G; Rindt C** (2002) The application of a 3D PTV algorithm to a mixed convection flow. *Exp Fluids* 33: 603-611.
- Koseff JR; Street RL** (1984) The lid-driven flow: A synthesis of qualitative and quantitative observations. *J Fluids Eng* 106: 390-398.
- Liao JI** (2002) Trajectory and velocity determination by smoother. MSc Thesis, Department of Electrical Engineering, National Taiwan University.
- Lo DC; Murugesan K; Young DL** (2005) Numerical solutions of three-dimensional velocity-vorticity Navier-Stokes equations by finite difference method. *Int J Numer Meth Fluids* 47: 1469-1487.
- Maas HG; Gruen A; Papantoniou D** (1993) Particle tracking velocimetry in three-dimensional flows. Part 1: Photogrammetric determination of particle coordinates. *Exp Fluids* 15: 133-146.
- Matas J-P; Morris JF; Gauzzelli E** (2004) Inertial migration of rigid spherical particles in Poiseuille flow. *J Fluid Mech* 515: 171-195.
- Migeon C** (2002) Details on the start-up development of the Taylor-Gortler-like vortices inside a square-section lid-driven cavity for $1,000 < Re < 3,200$. *Exp Fluids* 33: 594-602.
- Murugesan K; Lo DC; Young DL** (2005) An efficient global matrix free finite element algorithm for 3D flow problems. *Comm Numer Meth Eng* 21(3): 107-118.
- Pan F; Acrivos A** (1967) Steady flows in rectangular cavities. *J Fluid Mech* 28: 643-655.
- Segré G; Silberberg A** (1962) Behaviour of macroscopic rigid spheres in Poiseuille flow Part 2. Experimental results and interpretation. *J Fluid Mech* 14: 136-157.
- Shah M; Rangarajan K; Tsai PS** (1993) Motion trajectories. *IEEE Trans Syst Man Cybern* 23(4): 1138-1150.
- Shankar PN; Deshpande MD** (2000) Fluid mechanics in the driven cavity. *Annu Rev Fluid*

Mech 32: 93-136.

Spinewine B; Capart H; Larcher M; Zech Y (2003) Three-dimensional Voronoï imaging methods for the measurement of near-wall particulate flows. *Exp Fluids* 34: 227-241.

Ushijima S; Tanaka N (1996) Three-dimensional particle tracking velocimetry with laser-light sheet scannings. *J Fluids Eng* 118: 352-357.

Veber P; Dahl J; Hermansson R (1997) Study of the phenomena affecting the accuracy of a video-based particle tracking velocimetry technique. *Exp Fluids* 22: 482-488.

Virant M; Dracos T (1997) 3D PTV and its application on Lagrangian motion. *Meas Sci Technol* 8: 1539-1552.

Welch G; Bishop G (2001) An introduction to the Kalman filter. Course 8, SIGGRAPH 2001, Los Angeles, August 2001, ACM.

Figure captions

Figure 1. Experimental setup: **a** overall view; **b** sketch of the imaging configuration including DV camera, mirror system, and back-illumination rig; **c** side view of the lid-driven cavity; **d** front view.

Figure 2. Particle positioning in the image plane: **a** artificial long exposure image obtained from a sequence of 410 frames; **b** particle positions associated with the front view (+) and side view (\times), corresponding respectively to the left and right halves of the image. Two solid particles are present in this experiment.

Figure 3. Three-dimensional vector geometry of the stereo imaging configuration.

Figure 4. Three-dimensional positions of the two particles of Fig. 2, obtained by stereo ray matching. A conspicuous mismatched outlier is circled near the lower left hand corner.

Figure 5. Three-dimensional motions of a single suspended particle in the lid-driven cavity flow. The three panels show time series of the x -, y - and z -coordinates, respectively, as measured by the stereo methods (before Kalman filtering). Gray boxes outlines zones examined in detail in the next figures.

Figure 6. Zoom on portions of the position time series of Fig. 5. Dots: stereo data; thin line: signal obtained after a single forward pass of the Kalman filter, exhibiting an undesirable time shift to the right; thick line: signal resulting from a combination of forward and backward passes.

Figure 7. Kalman filter results for different values of ratio $\beta = \sigma \Delta t / \varepsilon$ representing the strength of the measurement error noise relative to the physical signal noise. Dots: raw data; thin line: $\beta = 0.005$; dashed line: $\beta = 0.025$; thick line: $\beta = 0.2$.

Figure 8. Tuning criterion for ratio β : the value selected is the one yielding a mean-squared difference between $\bar{\mathbf{x}}_k(\beta)$ and \mathbf{y}_k equal to the known noise variance ε^2 .

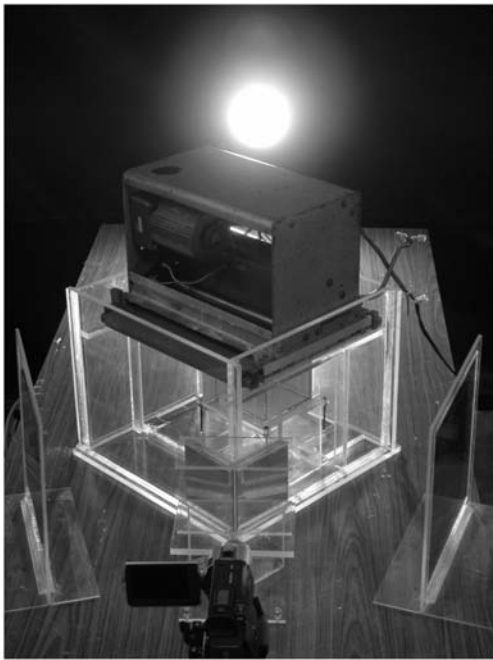
Figure 9. Time series of the three components of the filtered position $\bar{\mathbf{x}}$ of a single particle.

The shaded regions correspond to the start-up and typical cycle regime segments examined in greater detail in the next figures.

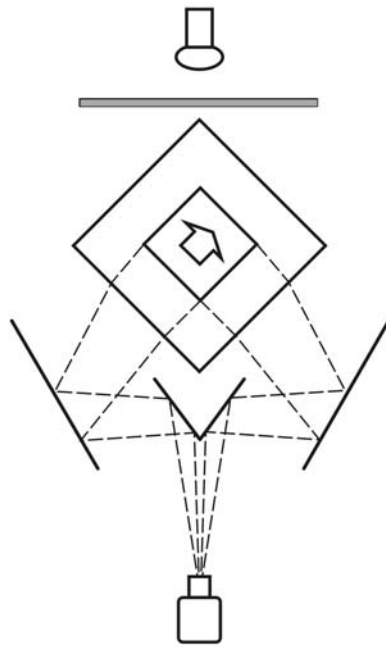
Figure 10. Three-dimensional trajectory of a suspended solid particle in the lid-driven cavity flow ($Re = 470$). Segment of 23 seconds immediately following the sudden start-up of the conveyor belt. **a** side view; **b** front view; **c** top view; **d** three-dimensional plot.

Figure 11. Three-dimensional trajectory of a suspended solid particle in the lid-driven cavity flow ($Re = 470$). Typical orbital cycle over a span of 43 seconds. **a** side view; **b** front view; **c** top view; **d** three-dimensional plot.

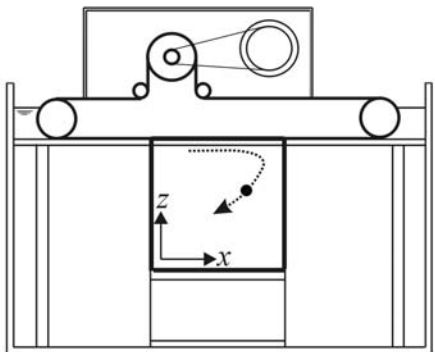
Figure 12. Simultaneous orbits of 10 suspended solid particles in the right half of the lid-driven cavity ($Re = 1030$), over a span of 17 seconds. **a** long exposure image obtained from a sequence of 500 frames; **b** three-dimensional plot; **c** front view; **d** side view.



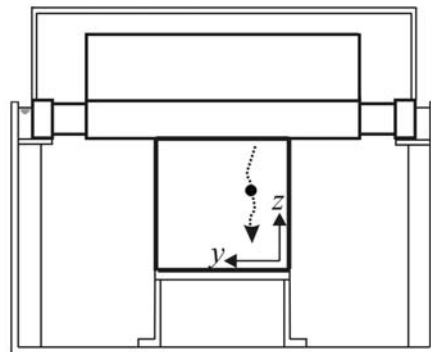
a



b

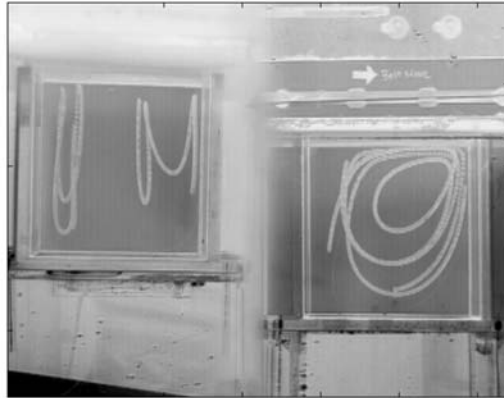


c

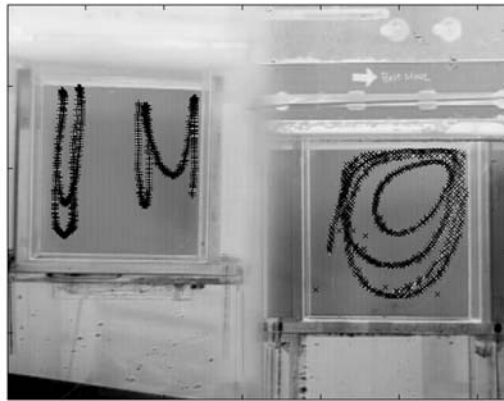


d

Figure 1



a



b

Figure 2

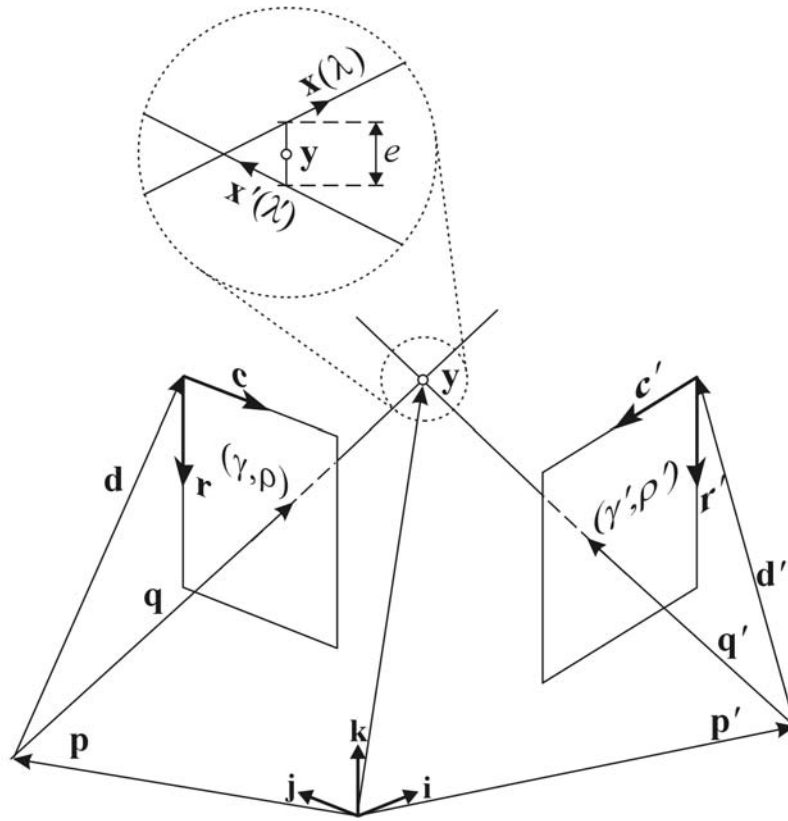


Figure 3

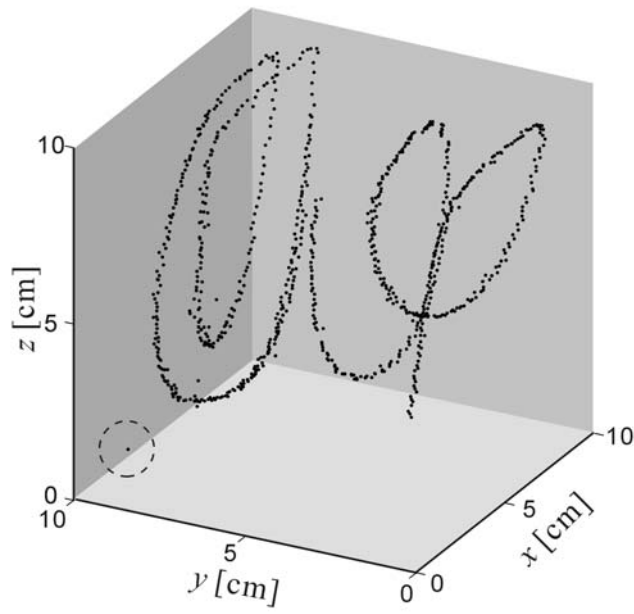


Figure 4

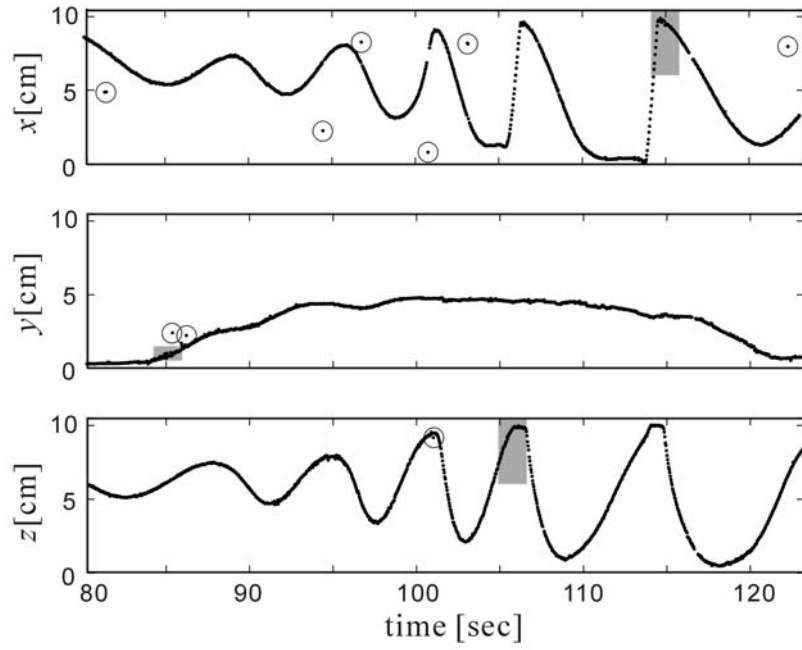


Figure 5

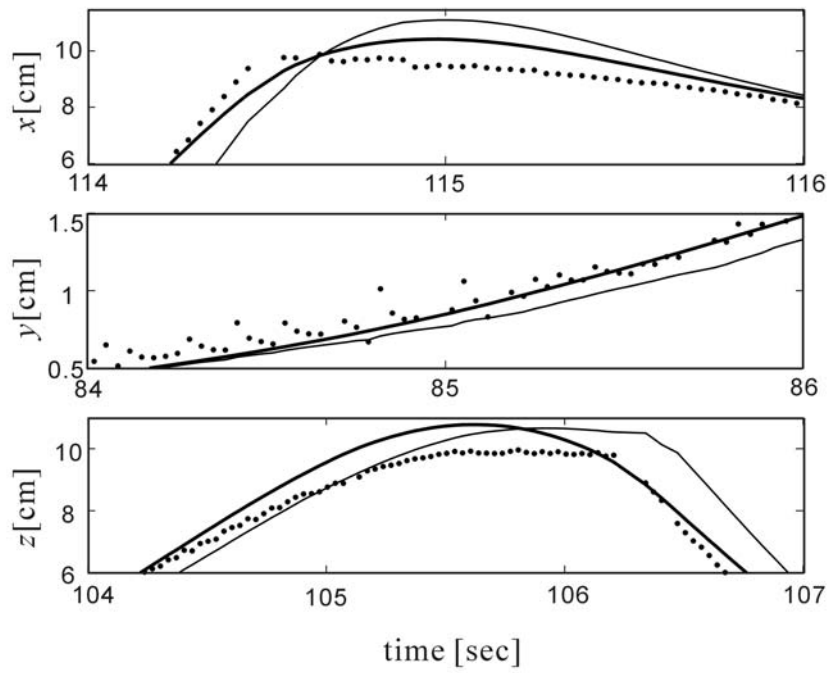


Figure 6

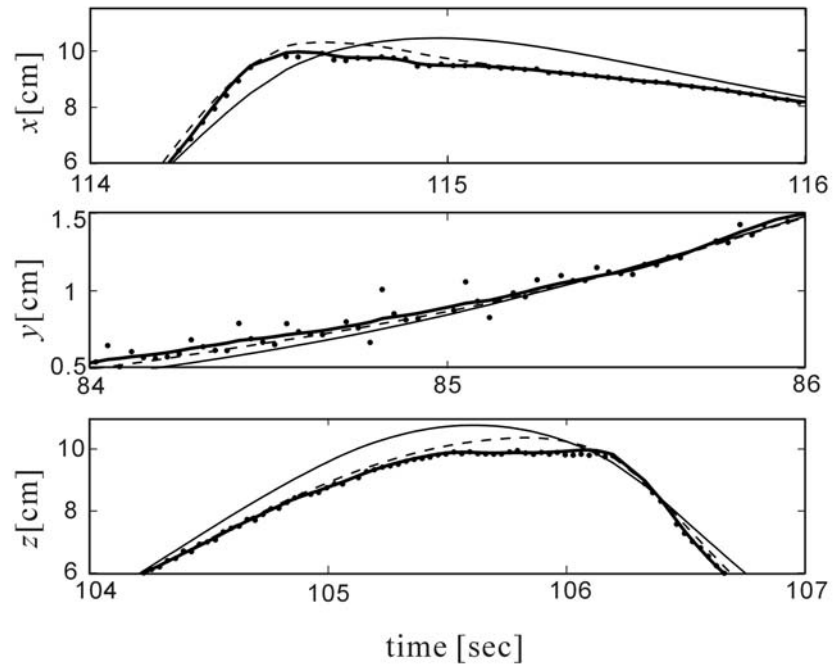


Figure 7

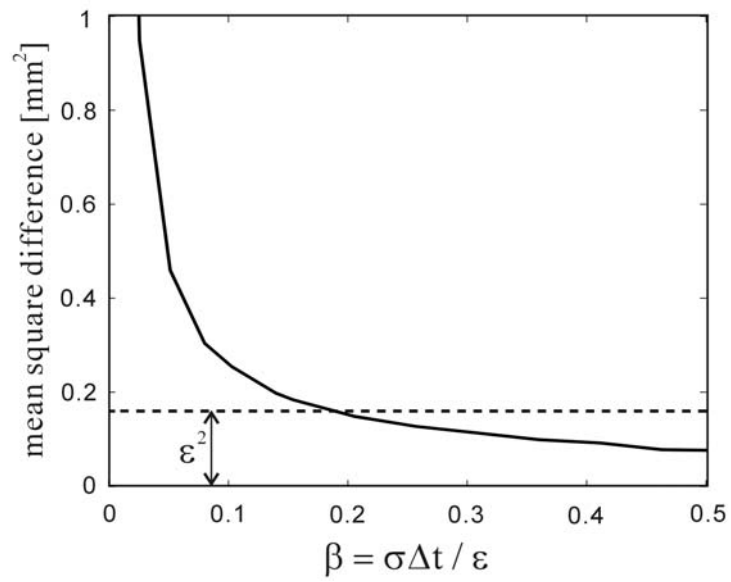


Figure 8

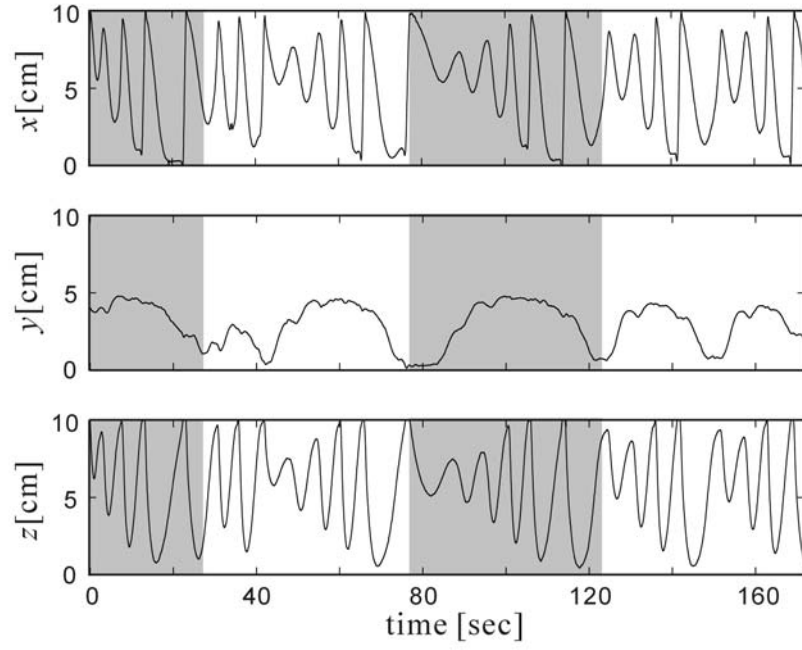


Figure 9

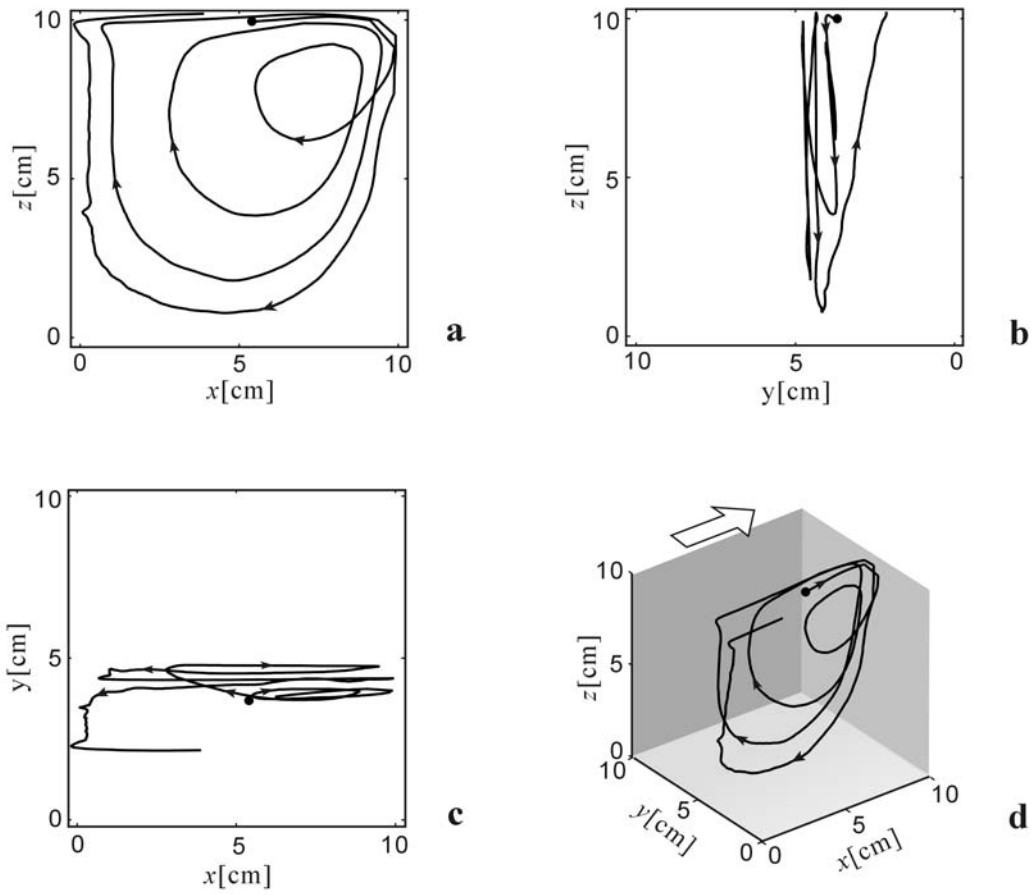


Figure 10

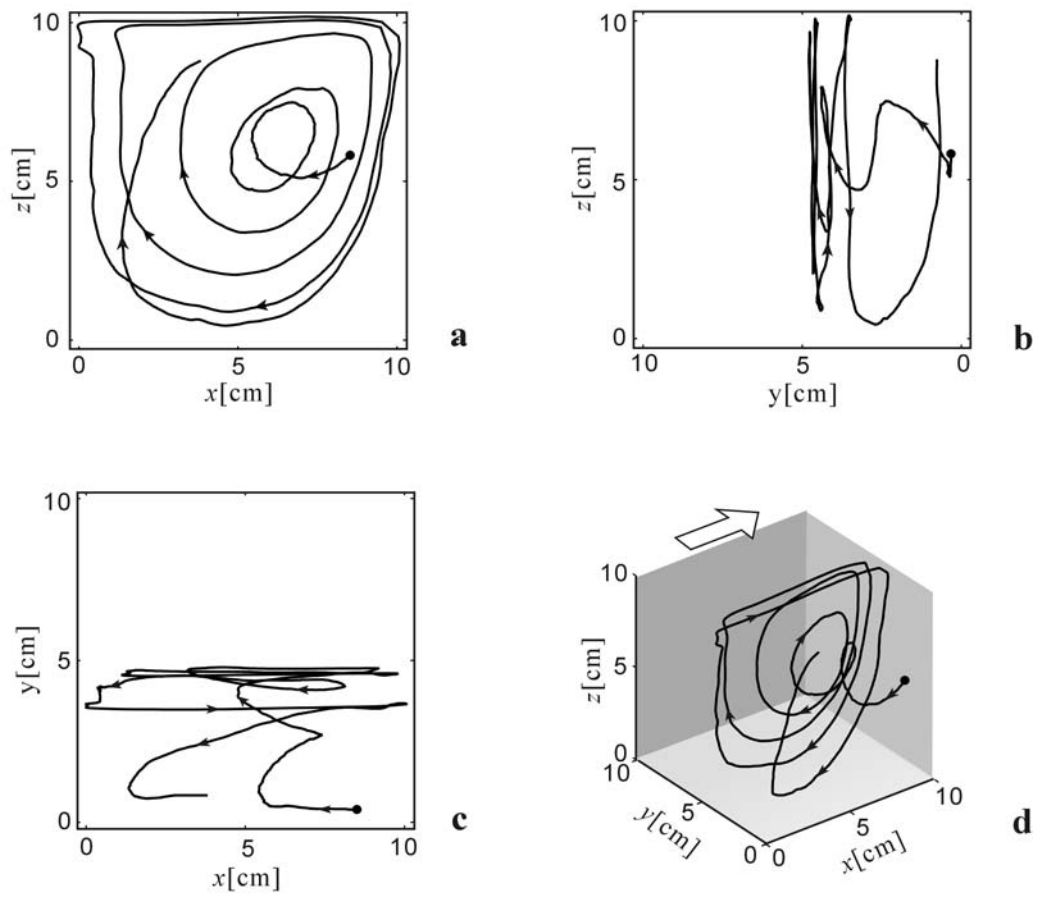
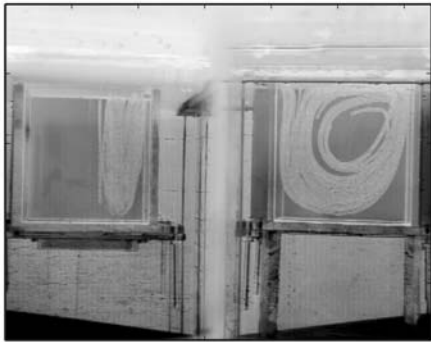
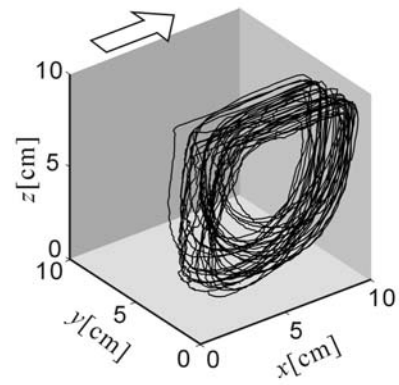


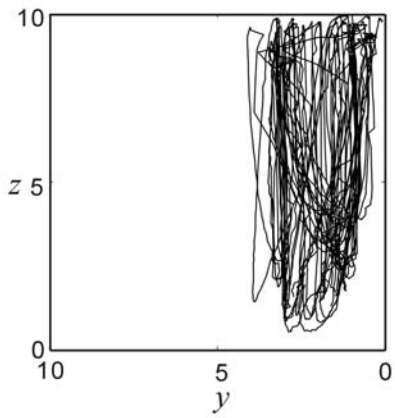
Figure 11



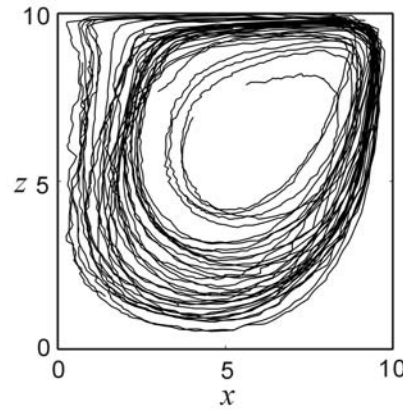
a



b



c



d

Figure 12

Numerical solution of three-dimensional velocity–vorticity Navier–Stokes equations by finite difference method

D. C. Lo, K. Murugesan and D. L. Young^{*,†}

Department of Civil Engineering and Hydrotech Research Institute, National Taiwan University, Taipei, Taiwan

SUMMARY

This paper describes the finite difference numerical procedure for solving velocity–vorticity form of the Navier–Stokes equations in three dimensions. The velocity Poisson equations are made parabolic using the false-transient technique and are solved along with the vorticity transport equations. The parabolic velocity Poisson equations are advanced in time using the alternating direction implicit (ADI) procedure and are solved along with the continuity equation for velocities, thus ensuring a divergence-free velocity field. The vorticity transport equations in conservative form are solved using the second-order accurate Adams–Bashforth central difference scheme in order to assure divergence-free vorticity field in three dimensions. The velocity and vorticity Cartesian components are discretized using a central difference scheme on a staggered grid for accuracy reasons. The application of the ADI procedure for the parabolic velocity Poisson equations along with the continuity equation results in diagonally dominant tri-diagonal matrix equations. Thus the explicit method for the vorticity equations and the tri-diagonal matrix algorithm for the Poisson equations combine to give a simplified numerical scheme for solving three-dimensional problems, which otherwise requires enormous computational effort. For three-dimensional-driven cavity flow predictions, the present method is found to be efficient and accurate for the Reynolds number range $100 \leq Re \leq 2000$. Copyright © 2004 John Wiley & Sons, Ltd.

KEY WORDS: finite difference method; ADI; TDMA; velocity–vorticity formulation; Navier–Stokes equations; staggered grid

1. INTRODUCTION

Numerical methods that are used to simulate incompressible viscous flows can be classified into three major categories, namely primitive variable (velocity–pressure) [1–5] formulation, stream function vector [6, 7] or vorticity–vector–potential [8] formulation and velocity–vorticity

*Correspondence to: D. L. Young, Department of Civil Engineering and Hydrotech Research Institute, National Taiwan University, Taipei, Taiwan.

†E-mail: dlyoung@hy.ntu.edu.tw

Contract/grant sponsor: NSC, Taiwan

Received 29 March 2003

Revised 12 August 2004

Accepted 14 October 2004

[9–16] formulation. The above formulations have been thoroughly investigated by various researchers for 2D and 3D flow problems using different numerical methods. Goda [17] simulated two- and three-dimensional cavity flows using the finite difference method. The major notion of his algorithm is to deal with only one-dimensional forms for both velocity and pressure calculations in spite of the three-dimensional equations. Elshabka and Chung [6] used the finite element method to solve the fourth-order vector partial differential equations for the solution of three-dimensional stream function vector components. Weinan and Liu [8] adopted an efficient and accurate finite difference method to calculate three-dimensional unsteady viscous incompressible flows in terms of the vorticity-vector-potential formulation on non-staggered grids. In the past couple of decades, the velocity–vorticity formulation has been investigated by many researchers using various numerical schemes such as the finite difference method [18, 19], the finite element method [9, 20] and the boundary element method (BEM) [10, 11].

The velocity–vorticity form of Navier–Stokes equations pioneered by Fasel [21] has provided an effective formulation for the solution of two-dimensional computational fluid dynamics (CFD) problems. Orlandi [22] established a numerical scheme for flow over a two-dimensional backward facing step using a block alternating direction implicit (ADI) method. Liu [23] and Napolitano and Pascazio [24] among others, used the finite difference method with a staggered grid to study three-dimensional-driven cavity flow problems. Two-dimensional velocity–vorticity formulation using the finite element method was first reported by Guevremont *et al.* [25]. They used quadratic finite elements for the velocity components and linear finite elements for the vorticity components. They also reported results for three-dimensional-driven cavity flow for $Re = 100$ and 400 . Recently Wong and Baker [9] developed a parallel solution algorithm for the solution of three-dimensional incompressible Navier–Stokes equations in velocity–vorticity form using the finite element method. They used Taylor’s series expansion scheme to obtain second-order accurate vorticity boundary conditions at the wall boundary. Young *et al.* [10] used the Eulerian–Lagrangian BEM (ELBEM) for the solution of two-dimensional incompressible viscous flow problems using velocity–vorticity formulation. The above method is obtained by the combination of the Eulerian–Lagrangian method and the BEM. The Poisson-type velocity equations are solved using the general boundary integral method with domain integration for the source terms and the vorticity boundary conditions are exactly determined. The vorticity transport equation is solved using the ELBEM on a transformed characteristic domain. Young *et al.* [11] also provided a combined boundary element and finite element method for the numerical solution of three-dimensional incompressible viscous flow using velocity–vorticity formulation. The use of finite difference or finite element method for three-dimensional flow problems demands large computational effort in time and in computer memory especially for solving problems of high Reynolds number flows. Continuous research is going on in the field of computational fluid dynamics to develop simplified numerical procedures for the solution of three-dimensional flow problems, so that even a personal computer could be used for dealing with high Reynolds number flow. The present work concentrates to contribute in that direction.

The numerical scheme followed to solve the three-dimensional velocity–vorticity equations using the finite difference technique can be described by the following numerical procedures:

- (1) The velocity Poisson equations obtained as a result of taking curl of the vorticity definition along with the continuity equation are made parabolic using the false-transient technique [18, 24, 26, 27] and hence they are accurately solved only at steady state.

- (2) The velocity Poisson equations are integrated in the time domain using a scalar ADI procedure, which reduces the equations to a diagonally dominant tri-diagonal matrix. Hence a simple tri-diagonal matrix algorithm (TDMA) can be used to solve the equations for velocities.
- (3) Procedure (2) is used to obtain velocities u and v in the x and y directions respectively. The velocity w in the z direction is obtained from the differentiated form of the continuity equation, thus assuring a divergence-free velocity field.
- (4) The Adams–Bashforth method, which is explicit and second-order accurate in time, is used to discretize the vorticity transport equations in time. The conservative form of the vorticity transport equations are used in order to satisfy the divergence-free constraint for the vorticity field in three dimensions.
- (5) The velocity and the vorticity variables in the Cartesian co-ordinates are discretized in space using a second-order accurate central difference scheme on an MAC staggered grid. The use of a staggered grid also ensures the accurate predictions of the field variables.
- (6) The use of the TDMA algorithm for the velocity Poisson equations and an explicit time marching scheme for the vorticity transport equations have enabled us to use the Gauss elimination technique for the solution of the field variables.
- (7) The above-simplified numerical solution procedure for the coupled governing equations has allowed us to employ a uniform mesh of size $101 \times 101 \times 101$ for obtaining the flow field for $Re = 2000$ using a Pentium-IV personal computer.
- (8) As far as the vorticity boundary conditions at the wall are concerned, a second-order accurate central difference scheme is adopted to calculate the vorticity from its definition.

The contents of the paper are organized as follows: Section 2 presents the vorticity transport equations and the velocity Poisson equations. Section 3 gives the details about the finite difference numerical procedure for the solution of the governing equations in velocity–vorticity form. The numerical results for a lid-driven cubical cavity flow for $Re = 100, 400, 1000$ and 2000 are discussed in Section 4. The accuracy of the results predicted by the present numerical scheme are verified and compared with the results of other numerical schemes. Section 5 contains our main conclusions.

2. GOVERNING EQUATIONS

The partial differential equations governing the viscous, laminar flow of an incompressible fluid are given by the Navier–Stokes equations. The corresponding non-dimensional form of the governing equations for conservation of mass and momentum can be expressed in vector form as [28]:

Continuity equation

$$\nabla \cdot \mathbf{u} = 0 \quad (1)$$

Momentum equation

$$\frac{\partial \mathbf{u}}{\partial t} + \mathbf{u} \cdot \nabla \mathbf{u} = -\nabla p + \frac{1}{Re} \nabla^2 \mathbf{u} \quad (2)$$

where \mathbf{u} is the velocity vector of the flow field, p is the pressure, $Re = uL/\nu$ is the Reynolds number and t is the time. Equations (1) and (2) represent the Navier–Stokes equations in the primitive variable (pressure–velocity) form.

By using the curl operator to Equation (2), one gets the following dimensionless form of the vorticity transport equation:

$$\frac{\partial \boldsymbol{\omega}}{\partial t} + \mathbf{u} \cdot \nabla \boldsymbol{\omega} = \boldsymbol{\omega} \cdot \nabla \mathbf{u} + \frac{1}{Re} \nabla^2 \boldsymbol{\omega} \quad (3)$$

where the vorticity vector $\boldsymbol{\omega}$ is defined as

$$\boldsymbol{\omega} = \nabla \times \mathbf{u} \quad (4)$$

By taking the curl of Equation (4) and using the continuity equation (1), the following velocity Poisson equation can be obtained:

$$\nabla^2 \mathbf{u} = -\nabla \times \boldsymbol{\omega} \quad (5)$$

Equations (3) and (5) are the velocity–vorticity form of the Navier–Stokes equations, with three equations for the velocity vector, $\mathbf{u} = (u, v, w)$ and three equations for the vorticity vector, $\boldsymbol{\omega} = (\xi, \eta, \varsigma)$ in the Cartesian co-ordinates.

We seek a solution for the field variables in the domain Ω , which satisfies the initial conditions,

$$u = u_0, v = v_0, w = w_0 \text{ at } t = 0 \quad (6)$$

and non-slip boundary conditions of velocity on the solid boundary Γ of Ω . The boundary condition for Equation (3) is obtained by using the vorticity definition of Equation (4) on the boundary.

3. FINITE DIFFERENCE NUMERICAL SCHEME

The solenoidality constraint on the vorticity field in three-dimension requires a solution of the system of governing equations represented by Equations (3) and (5) with boundary conditions given by Equations (4) and (6). However, the computation of the six field variables in a 3D domain using a direct solver is an arduous challenge. The solution of the time-dependent vorticity transport equations (3) and the elliptic Poisson equations (5) necessarily demands the use of a direct solver. The solution procedure can be simplified by making the velocity Poisson equations (5) also parabolic. This can be achieved by making use of the false-transient method proposed by Mallinson and Davis [26]. With this modification, the parabolic form of the velocity Poisson equations (5) can be expressed as

$$\alpha \frac{\partial \mathbf{u}}{\partial t} - \nabla^2 \mathbf{u} - \nabla \times \boldsymbol{\omega} = 0 \quad (7)$$

where α is a relaxation parameter. It is obvious that the steady state solutions for the flow field are obtained when the time derivatives in Equations (3) and (7) approach zero. A simple ADI algorithm can be adopted to discretize the time derivatives in Equation (7). Considering

the first component of the kinematic relations (7), it can be rewritten as a tri-diagonal system of equations of the form

$$a_i u_{i-1,j,k} + b_i u_{i,j,k} + c_i u_{i+1,j,k} = d_i \quad (8)$$

where

$$a_i = -\frac{\Delta t}{\alpha \Delta x^2}$$

$$b_i = 1 + \frac{2\Delta t}{\alpha \Delta x^2}$$

$$c_i = -\frac{\Delta t}{\alpha \Delta x^2}$$

$$d_i = R(u_{i,j,k})$$

and $R(u_{i,j,k})$ is the residual of the discretized form of the parabolic equation (7) [12]. This procedure yields $N_j \times N_k$ linear system of equations of the type given by Equation (8). Initially the velocities u and v are calculated by adopting the ADI procedure and then the velocity w is calculated from the continuity equation as given below:

$$\frac{\partial^2 w}{\partial z^2} = -\frac{\partial}{\partial z} \left(\frac{\partial u}{\partial x} + \frac{\partial v}{\partial y} \right) \quad (9)$$

Since the velocities u and v are already known the resulting set of equations from Equation (9) can be solved using the TDMA. The main advantage of the present numerical solution procedure is that it assures a divergence-free solution for the velocity field, in addition to achieving a higher numerical accuracy and a significant reduction in the computational time.

The vorticity transport equations (3) are discretized in time using the explicit, second-order accurate Adams–Bashforth scheme. The discretized form of the vorticity transport equations (3) for the three vorticity components in the Cartesian co-ordinates can be written as

$$\frac{\zeta^{n+1} - \zeta^n}{\Delta t} + 1.5 f_1^n - 0.5 f_1^{n-1} = 0 \quad (10)$$

$$\frac{\eta^{n+1} - \eta^n}{\Delta t} + 1.5 f_2^n - 0.5 f_2^{n-1} = 0 \quad (11)$$

$$\frac{\varsigma^{n+1} - \varsigma^n}{\Delta t} + 1.5 f_3^n - 0.5 f_3^{n-1} = 0 \quad (12)$$

where

$$f_1 = \frac{\delta_y}{\Delta y} (v\zeta) + \frac{\delta_z}{\Delta z} (w\zeta) - \frac{\delta_y}{\Delta y} (\eta u) - \frac{\delta_z}{\Delta z} (\varsigma u) - \frac{1}{Re} \left(\frac{\delta^2}{\Delta x^2} + \frac{\delta^2}{\Delta y^2} + \frac{\delta^2}{\Delta z^2} \right) \zeta$$

$$f_2 = \frac{\delta_x}{\Delta x} (u\eta) + \frac{\delta_z}{\Delta z} (w\eta) - \frac{\delta_x}{\Delta x} (\xi v) - \frac{\delta_z}{\Delta z} (\varsigma v) - \frac{1}{Re} \left(\frac{\delta^2}{\Delta x^2} + \frac{\delta^2}{\Delta y^2} + \frac{\delta^2}{\Delta z^2} \right) \eta$$

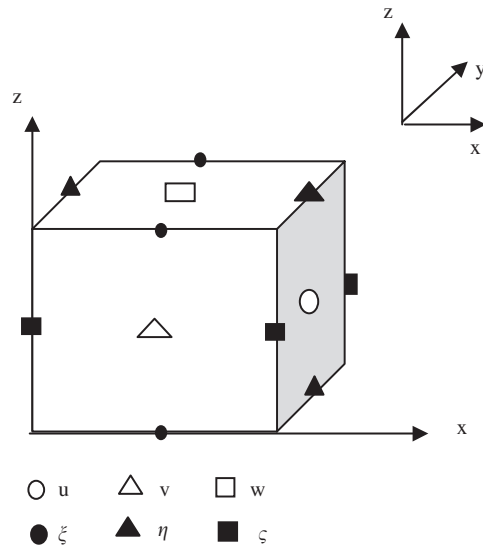


Figure 1. Three-dimensional staggered grid.

$$f_3 = \frac{\delta_x}{\Delta x}(u\zeta) + \frac{\delta_y}{\Delta y}(v\zeta) - \frac{\delta_x}{\Delta x}(\xi w) - \frac{\delta_y}{\Delta y}(\eta w) - \frac{1}{Re} \left(\frac{\delta^2}{\Delta x^2} + \frac{\delta^2}{\Delta y^2} + \frac{\delta^2}{\Delta z^2} \right) \zeta$$

and $\delta_x, \delta_y, \delta_z$ are the first-order central difference operators, $\delta_x^2, \delta_y^2, \delta_z^2$ are the second-order central difference operators. In order to ensure accuracy in the prediction of velocities and vorticities, a MAC staggered grid system as displayed in Figure 1 is used in the present numerical scheme. The final form of the discretized equations (8) and (10)–(12) for velocities and vorticities, respectively, are second-order accurate in time and space. The numerical stability conditions are satisfied by using the conservative form of the vorticity transport equations in the discretized form as expressed by Equations (10)–(12) and using a time step calculated based on the following numerical stability condition:

$$\left| \frac{u_{\max} \Delta t}{\Delta x} \right| \leq 1, \left| \frac{v_{\max} \Delta t}{\Delta y} \right| \leq 1, \left| \frac{w_{\max} \Delta t}{\Delta z} \right| \leq 1 \tag{13}$$

$$\frac{\Delta t}{Re} \left(\frac{1}{\Delta x^2} + \frac{1}{\Delta y^2} + \frac{1}{\Delta z^2} \right) \leq \frac{1}{2} \tag{14}$$

4. MODEL APPLICATION

Traditionally, the velocity and pressure are treated as the primitive variables while analyzing a viscous incompressible flow problem. That means the Navier–Stokes equations (2) and the

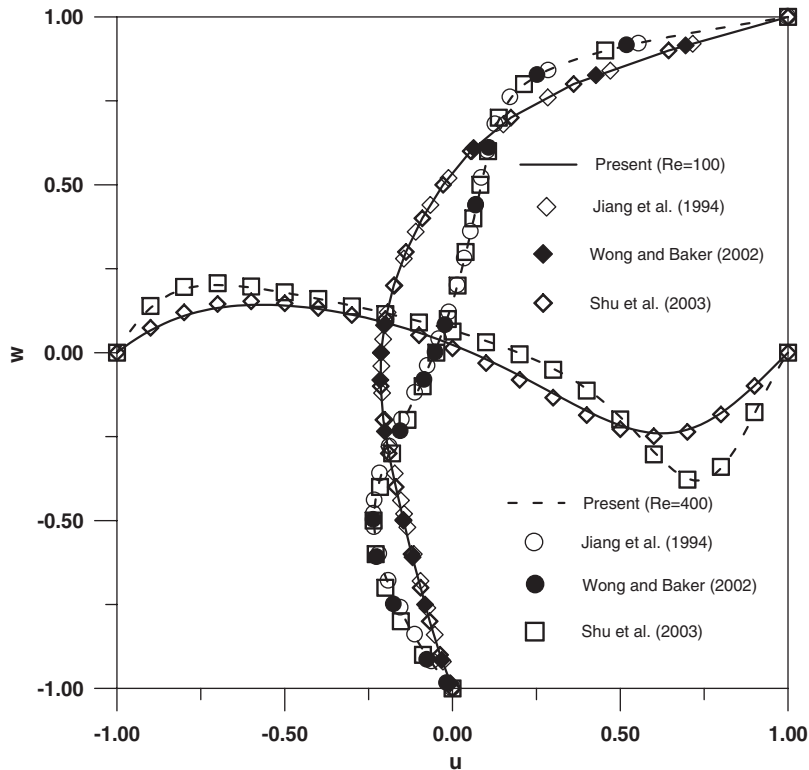


Figure 2. Velocity profiles for $Re = 100$ and 400 on vertical and horizontal centrelines.

continuity equation (1) should be taken into consideration simultaneously. However, while solving these two sets of equations, pressure and velocity are involved during the iterating process. However it is rather difficult to implicitly deal with the continuity equation because there is no pressure term in Equation (1). On the other hand, the velocity-vorticity formulation has no such problem because it is free from the pressure term. In the present model, the velocity Poisson equations are initially solved to get the velocity distribution. The vorticity boundary conditions are calculated using the vorticity definition for an initial guess of the wall vorticity boundary conditions.

The lid-driven cavity flow problem is always considered as a bench mark problem for testing any new numerical scheme. The present finite difference numerical procedure is validated by applying it to a cubical lid-driven cavity problem, in which the top wall is assumed to move parallel to the x -axis (refer Figure 1) with constant velocity of unity (dimensionless). The fluid in the cavity is assumed to be viscous and incompressible. In the present work, results were obtained for the lid-driven cavity flow for $Re = 100$ using a $51 \times 51 \times 51$ uniform mesh and for $Re = 400, 1000$ and 2000 using a uniform mesh of size $101 \times 101 \times 101$.

In the three-dimensional Navier-Stokes equations system, the intensity of the non-linearity, the diffusion and the convective effects are related with the magnitude of the Reynolds number. Therefore, fine meshes have to be used while solving high Reynolds number flows. Accurate

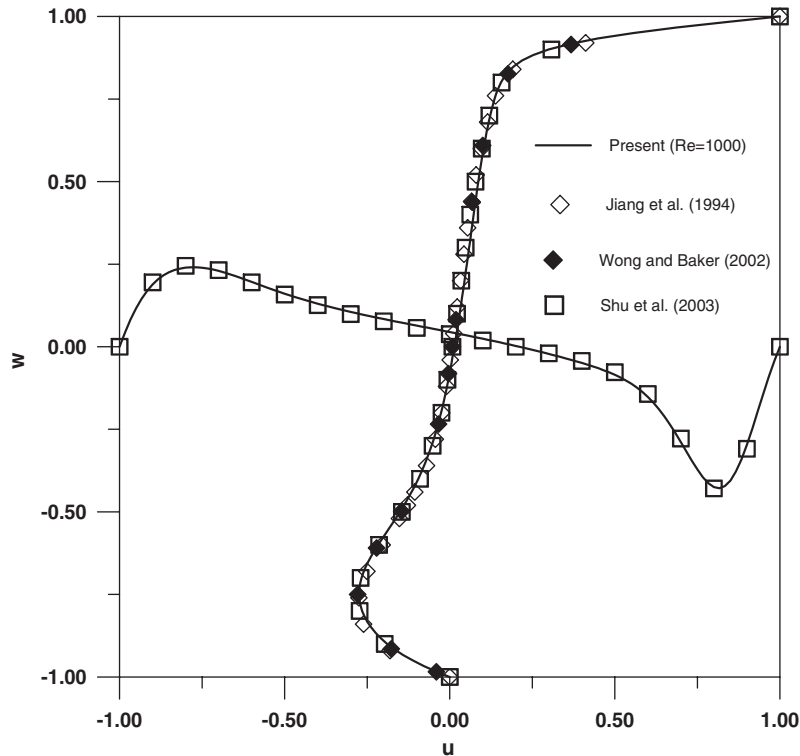


Figure 3. Velocity profiles for $Re = 1000$ on vertical and horizontal centrelines.

predictions for different Reynolds number flows can be obtained only by using an appropriate mesh. The results obtained are also strongly associated with the way in which the mesh size is adopted. We require to use a high-density mesh in the regions of steep gradients of the field variables, in order to capture the development of the boundary layer with increase in the Reynolds number. At low values of Reynolds number the diffusion plays a significant role in the formation of the flow field, however when the Reynolds number is increased to 100, the convection effects modify the diffusion process. In the present work the numerical results predicted for $Re = 100, 400, 1000$ and 2000 are discussed. All the computations have been carried out on a 1.5 GHz Pentium-IV personal computer with 256 Mb RAM.

The results obtained by the present numerical method for a 3D lid-driven cavity flow are presented in the form of velocity vectors and vorticity contours at the mid-planes along the principal axes of the cavity in order to understand the flow patterns at different Reynolds numbers. For the purpose of validation, the u velocity profile along the vertical central line ($u-z$ plot) and the w velocity profile along the horizontal central line ($x-w$ plot) of the cavity are compared with available results. Figures 2 and 3 show the $u-z$ comparisons with the results of Jiang *et al.* [29], Wong and Baker [9] and Shu *et al.* [30] and $x-w$ comparisons with the results of Shu *et al.* [30] for $Re = 100, 400$ and 1000 . The results predicted by the present scheme are in close agreement with the results of the above authors for $Re = 100,$

Table I. Comparison of maximum negative u velocity.

Re	Present		Reference [29]		Reference [9]	
	z	u	z	u	z	u
100	0.46	-0.2163	0.48	-0.212	0.4592	-0.2154
400	0.26	-0.2334	0.26	-0.2341	0.2509	-0.2349
1000	0.12	-0.2671	0.12	-0.2754	0.125	-0.2792

Table II. u velocity along the vertical centreline of the 3D-driven cavity.

z location	$Re = 100$	$Re = 400$	$Re = 1000$	$Re = 2000$
0	0	0	0	0
0.04	-0.02928	-0.0645	-0.15736	-0.16252
0.08	-0.05430	-0.11576	-0.23687	-0.2429
0.1	-0.06578	-0.13817	-0.25743	-0.26394
0.12	-0.07675	-0.15886	-0.26714	-0.26501
0.14	-0.08740	-0.17779	-0.26615	-0.24457
0.16	-0.09780	-0.19471	-0.25535	-0.21002
0.2	-0.11815	-0.22071	-0.21285	-0.13603
0.22	-0.12816	-0.22882	-0.18648	-0.10671
0.24	-0.13809	-0.23313	-0.15988	-0.08372
0.26	-0.14789	-0.23343	-0.13468	-0.06607
0.3	-0.16687	-0.22212	-0.09161	-0.04199
0.32	-0.17587	-0.21108	-0.07413	-0.03363
0.36	-0.19227	-0.1809	-0.0463	-0.02111
0.4	-0.20548	-0.1443	-0.02574	-0.01183
0.42	-0.21047	-0.12518	-0.01738	-0.00786
0.44	-0.21414	-0.10619	-0.00997	-0.00413
0.46	-0.21632	-0.08772	-0.00328	-0.00055
0.5	-0.21561	-0.05334	0.00856	0.0065
0.52	-0.21247	-0.03767	0.01399	0.01011
0.56	-0.20017	-0.00952	0.02434	0.01777
0.58	-0.19092	0.00306	0.0294	0.02191
0.64	-0.15073	0.03599	0.04476	0.036
0.66	-0.13324	0.04573	0.05008	0.04133
0.68	-0.11369	0.05505	0.05558	0.04697
0.72	-0.06807	0.07288	0.06723	0.05918
0.76	-0.01206	0.09045	0.08011	0.07255
0.78	0.02111	0.09954	0.08716	0.07967
0.8	0.05888	0.10919	0.0947	0.08713
0.84	0.15361	0.13287	0.11205	0.10339
0.88	0.28593	0.17537	0.1349	0.12264
0.9	0.37125	0.21562	0.15264	0.13468
0.92	0.47149	0.28139	0.18367	0.15167
0.94	0.58704	0.3865	0.24776	0.18533
0.96	0.71653	0.54381	0.38323	0.27562
0.98	0.85624	0.75538	0.63626	0.52063
1	1	1	1	1

Table III. w velocity along the horizontal centreline of the 3D-driven cavity.

x location	$Re = 100$	$Re = 400$	$Re = 1000$	$Re = 2000$
0	0	0	0	0
0.04	0.06358	0.11371	0.16087	0.1792
0.06	0.08845	0.14992	0.20336	0.21512
0.08	0.10899	0.17454	0.2265	0.2297
0.1	0.12547	0.18978	0.23616	0.2293
0.12	0.13825	0.19794	0.23647	0.21742
0.14	0.14767	0.20103	0.23013	0.19818
0.18	0.15784	0.19788	0.2057	0.15434
0.2	0.15927	0.19351	0.19092	0.13496
0.24	0.15627	0.18176	0.16154	0.10471
0.26	0.15232	0.17493	0.14795	0.09328
0.3	0.14041	0.16006	0.12362	0.07556
0.32	0.13272	0.15216	0.11279	0.06852
0.38	0.10370	0.12677	0.08438	0.05162
0.42	0.07977	0.10826	0.06779	0.04242
0.48	0.03708	0.07738	0.04487	0.03007
0.52	0.00388	0.05411	0.03027	0.02216
0.54	-0.01419	0.04147	0.02305	0.01816
0.56	-0.03326	0.02803	0.01583	0.01405
0.6	-0.07418	-0.00185	0.00114	0.00528
0.62	-0.09585	-0.01872	-0.00644	0.00049
0.64	-0.11811	-0.03729	-0.01431	-0.00464
0.66	-0.14066	-0.05797	-0.02259	-0.01018
0.68	-0.16315	-0.08129	-0.0315	-0.0162
0.72	-0.20578	-0.1381	-0.05266	-0.02986
0.74	-0.22454	-0.1725	-0.06632	-0.03766
0.76	-0.24048	-0.2111	-0.0837	-0.04627
0.78	-0.25264	-0.2527	-0.10686	-0.056
0.82	-0.26169	-0.3346	-0.18149	-0.08235
0.84	-0.25687	-0.36537	-0.23736	-0.10387
0.86	-0.24502	-0.38096	-0.30346	-0.1384
0.88	-0.22595	-0.37533	-0.3694	-0.19475
0.9	-0.19991	-0.34516	-0.41506	-0.27727
0.92	-0.16756	-0.29166	-0.41534	-0.36774
0.94	-0.12997	-0.22098	-0.3548	-0.40986
0.96	-0.08851	-0.14255	-0.2435	-0.34083
0.98	-0.04468	-0.0663	-0.11416	-0.17465
1	0	0	0	0

400 and 1000. The comparison of the minimum u velocity with the results of Jiang *et al.* [29] and Wong and Baker [9] for $Re = 100, 400$ and 1000 as given in Table I shows the present numerical scheme could predict the flow results with acceptable numerical error. The minimum u velocity calculated by Wong and Baker [9] is 0.2154 for $Re = 100$, compared to 0.2163 computed by the present study, with an error of 0.42%. The values of u velocity along the z direction and values of w velocity along the x direction for selected nodal points are given in Tables II and III, respectively, for $Re = 100, 400, 1000$ and 2000 . The efficiency of the present numerical scheme can be well appreciated by noting that the present results are obtained using entirely a different numerical scheme compared to Jiang *et al.* [29] who used

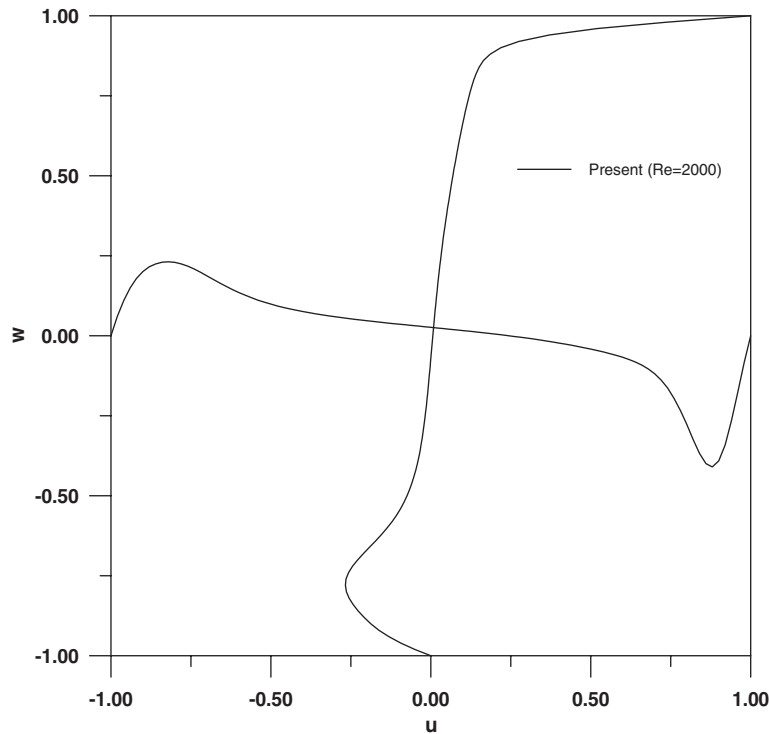


Figure 4. Velocity profiles for $Re=2000$ on vertical and horizontal centrelines.

the least square finite element method and Wong and Baker [9] who obtained results using eight-node hexahedral finite elements on a non-staggered grid. Having validated the code up to $Re = 1000$, results are obtained for $Re = 2000$ using a uniform grid of size $101 \times 101 \times 101$. The $u-z$ plot and $x-w$ plot for $Re = 2000$ are shown in Figure 4. The increase in the Reynolds number value from 1000 to 2000 has resulted in further thinning of the boundary layer near the moving wall as observed in Figure 4 by the sharp velocity gradient. Also it develops a dip in the $u-z$ velocity profile before reaching the minimum value.

The most important feature of 3D cavity flows is the end wall effect, which is not observed in the case of 2D cavity flows. The end wall effect produces different flow patterns resulting in the formation of eddies and vortices. This flow structure could be well understood by the velocity and vorticity contours projected on the mid-planes along the principal axes of the cavity. The velocity vectors projected on $y = 0.5$ plane for $Re = 100, 400, 1000$ and 2000 are shown in Figures 5(a), (b), (c) and (d), respectively. For $Re = 100$, the axis of the primary vortex starts at the right upper region of the cavity. The end wall effect causes the axis of the primary vortex to move towards the centre of the cavity with increase in Reynolds number as observed in the above figures. The span wise flow becomes more important at high Reynolds number for 3D cavity flows. The velocity vector plots on $x = 0.5$ plane shown in Figures 6(a)–(d) highlight the generation of secondary vortices at high Reynolds numbers. Initially two vortices are observed at the symmetric centre plane and the vortices start moving

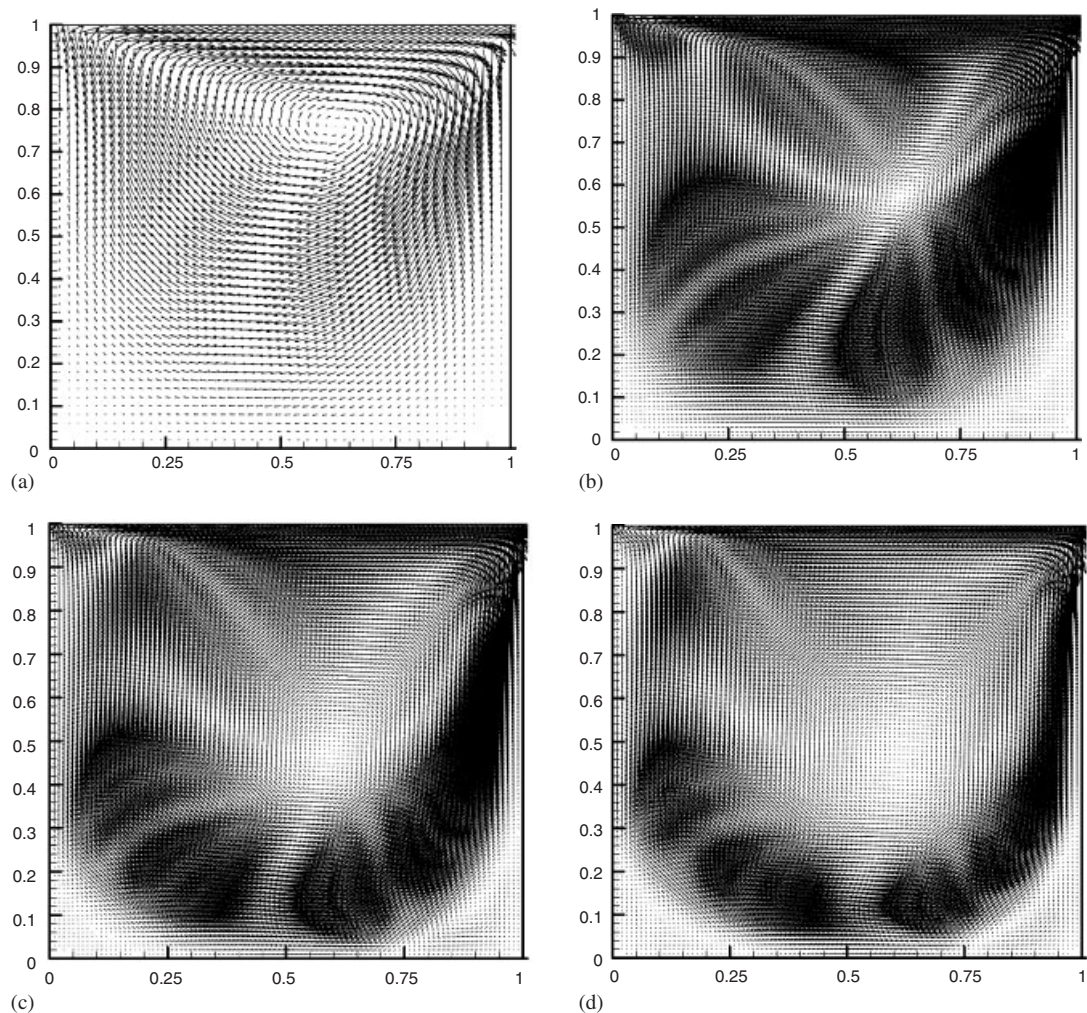


Figure 5. Velocity distribution at $y=0.5$ plane. (a) $Re=100$; (b) $Re=400$; (c) $Re=1000$; (d) $Re=2000$.

towards the bottom as well as the end of the sidewalls with increase in Reynolds number. At $Re=1000$, two recirculation cells also start appearing at the top ends of the sidewalls. The bottom vortices become strong at $Re=2000$ as observed in Figure 6(d). The modifications of the flow fields at $x=0.5$ plane for different Reynolds number is an important consequence of the three-dimensional effect. The velocity vectors on $z=0.5$ plane, which is parallel to the moving lid are shown in Figures 7(a)–(d) for $Re=100$ – 2000 . As the top lid moves in the positive x direction, the fluid is expected to take the opposite direction for the return flow as shown in Figure 7(a) for $Re=100$. With increase in Reynolds number, the smooth flow parallel to the x -axis is disturbed. Since the flow is already flowing span wise in the x - y

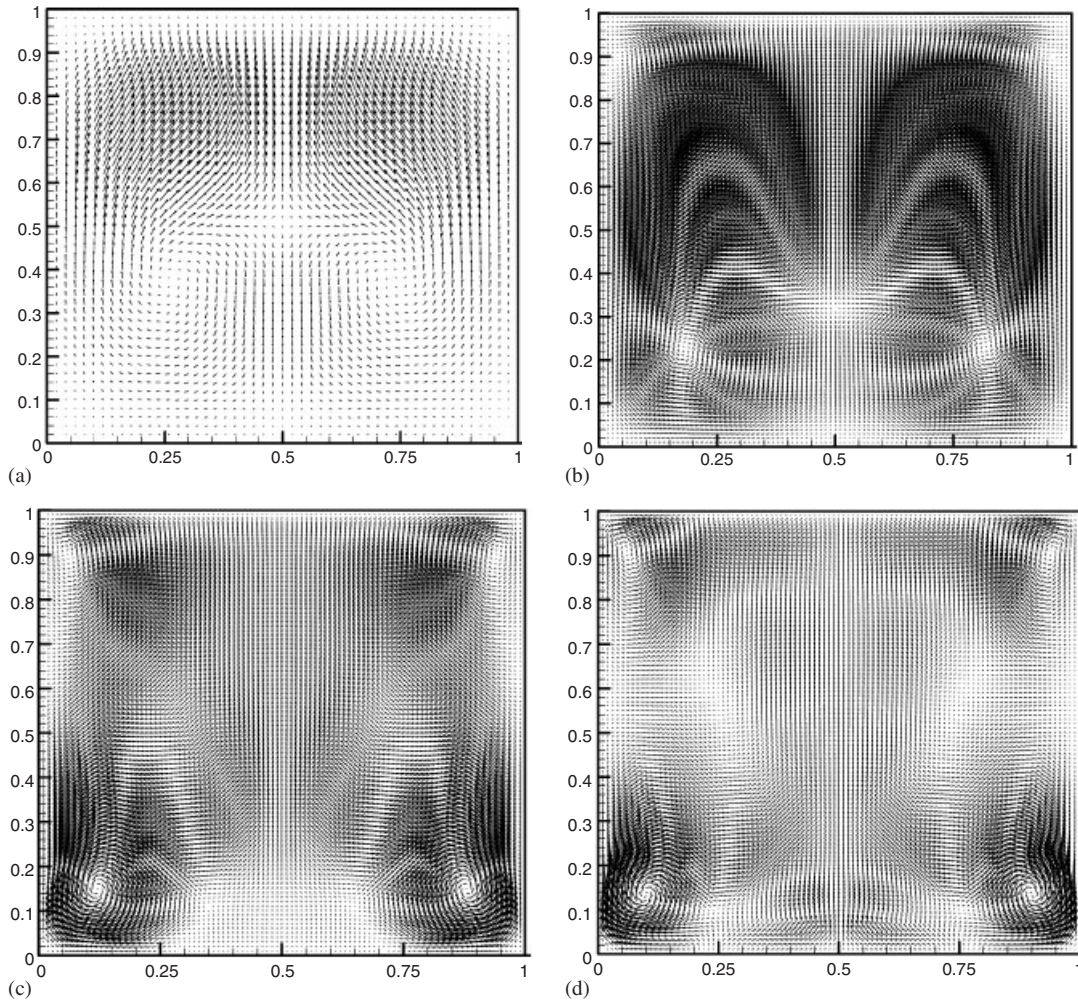


Figure 6. Velocity distribution at $x=0.5$ plane. (a) $Re=100$; (b) $Re=400$; (c) $Re=1000$; (d) $Re=2000$.

plane, the effect of increase in Reynolds number is to make the flow in the z direction as well, thus making the flow fully three-dimensional. This results in the generation of two more symmetric vortices to the left of the original vortices. As the Reynolds number increases the initial vortices start diffusing at the centre of the cavity, with the secondary vortices start moving continuously towards the end walls. At $Re=2000$, the secondary vortices also start merging along with the original vortices formed at the centre of the cavity. The velocity vectors projected on the centre planes of all the principal axes as illustrated in Figures 5–7, are in good qualitative agreement with the results of Wong and Baker [9] for $Re=100, 400$ and 1000 and with the results of Jiang *et al.* [29], Nikfetrat and Hafez [31], Ho and Lin [32] and Ku *et al.* [33] for $Re=100$ and 400 . Similar comparisons of the velocity vectors on

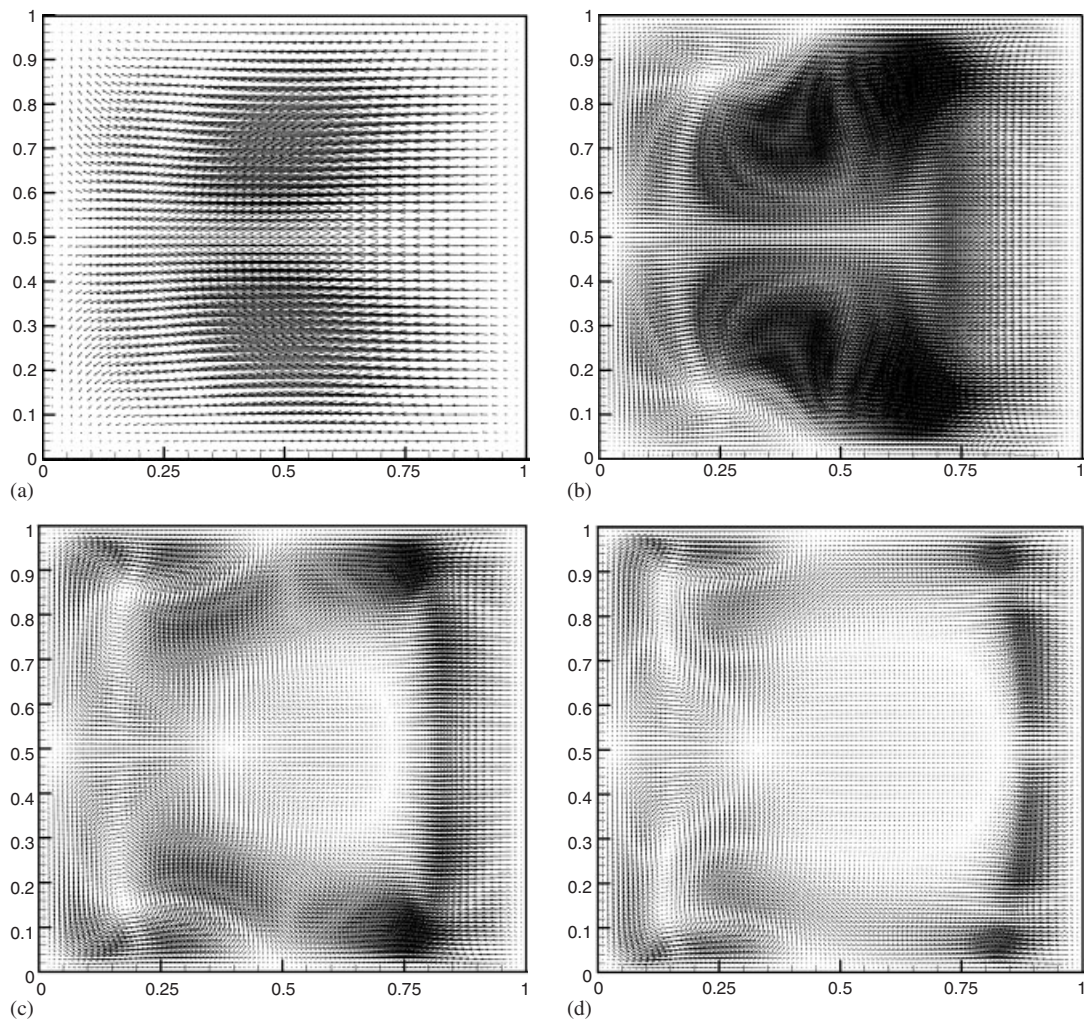


Figure 7. Velocity distribution at $z=0.5$ plane. (a) $Re=100$; (b) $Re=400$; (c) $Re=1000$; (d) $Re=2000$.

$y=0.5$ with the two-dimensional cavity flow results of Burggraf [34] and Ghia *et al.* [35] for $Re=100$ and 400, indicates that the present model could predict the flow patterns in a 3D cubic cavity for a wide range of Reynolds numbers.

For obtaining the solution for velocities the continuity equation is satisfied as shown by Equation (9). Also the conservative forms of the vorticity transport equations (10)–(12) are solved to obtain the vorticity components. Hence the divergence-free solutions for the velocities and the vorticities are ensured. Since we use the vorticity definition to compute the boundary vorticity values, the solenoidal condition on the vorticity field is also satisfied as stated by Guj and Stella [12]. This fact can be verified by plotting the vorticity values at different planes of the cavity. The y direction vorticity contours at $y=0.5$ plane for $Re=100$,

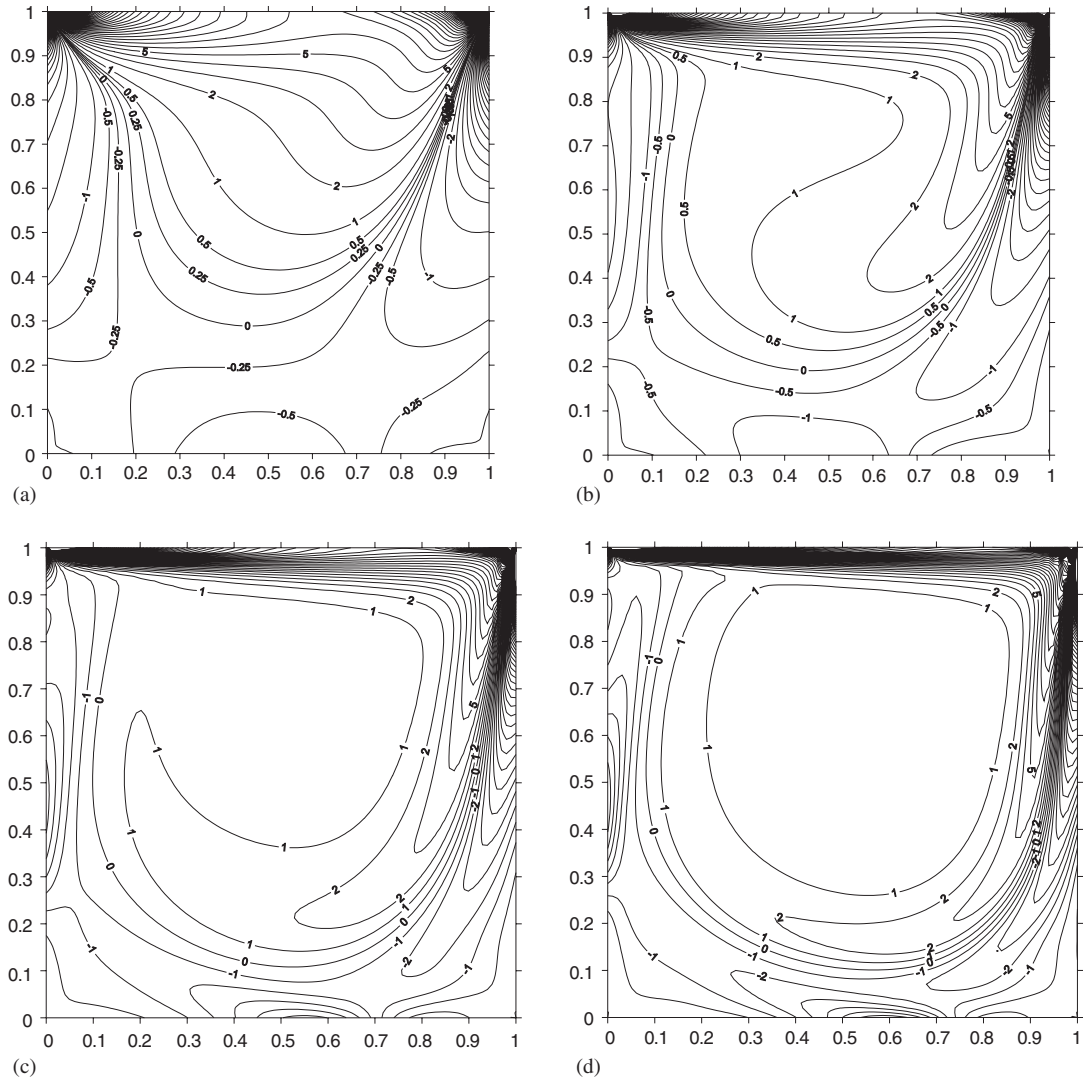


Figure 8. Vorticity (η) contour at $y=0.5$ plane. (a) $Re=100$; (b) $Re=400$; (c) $Re=1000$; (d) $Re=2000$.

400, 1000 and 2000 are shown in Figures 8(a), (b), (c) and (d), respectively. The symmetry of the vorticity contours, which are observed in the case of Stokes flow, is disturbed for high Reynolds numbers as the inertial forces become dominating over the viscous forces. The direction of distortion will be counter-clockwise since the top lid is moving from left to right. Figure 8(a) clearly indicates these distortions for $Re=100$. As the Reynolds number increases, the vorticity generated on the top wall and other boundary regions starts moving to other regions due to increase in the inertial forces as observed in Figures 8(b)–(d). These vortices

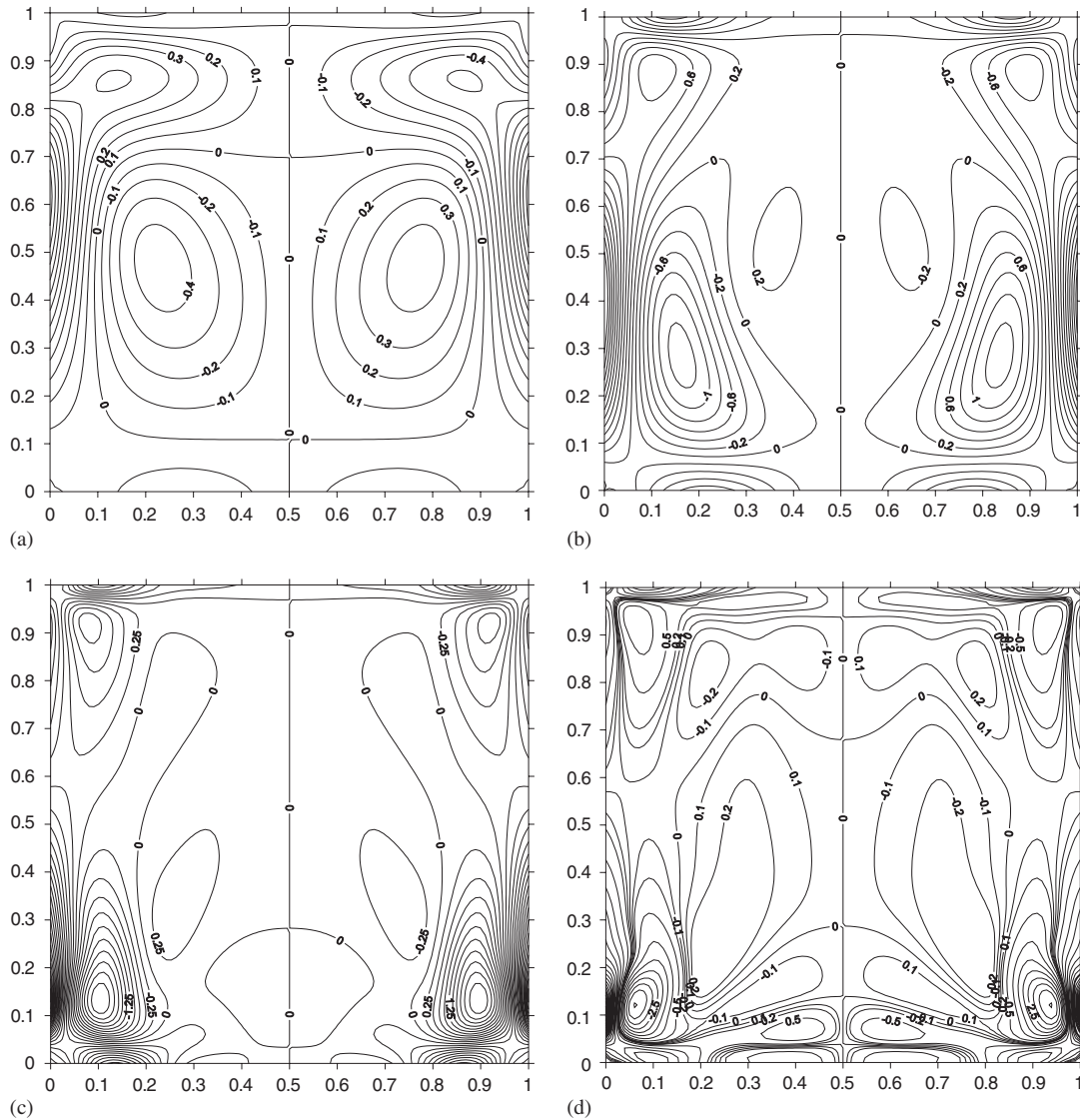


Figure 9. Vorticity (ζ) contour at $x=0.5$ plane. (a) $Re = 100$;
 (b) $Re = 400$; (c) $Re = 1000$; (d) $Re = 2000$.

try to form a flow pattern similar to solid rotation if they get sufficient strength. This type of flow pattern could not be captured up to $Re = 1000$. When the Reynolds number increases to 2000, most of the vortices near the centre of the cavity have closed themselves, thus forming a flow pattern of solid rotation at the centre, as shown in Figure 8(d). In order to observe the 3D effect, the x direction vorticity contours at $x = 0.5$ plane for different Reynolds numbers are shown in Figures 9(a)–(d). At moderate Reynolds numbers, the secondary vortices are not ob-

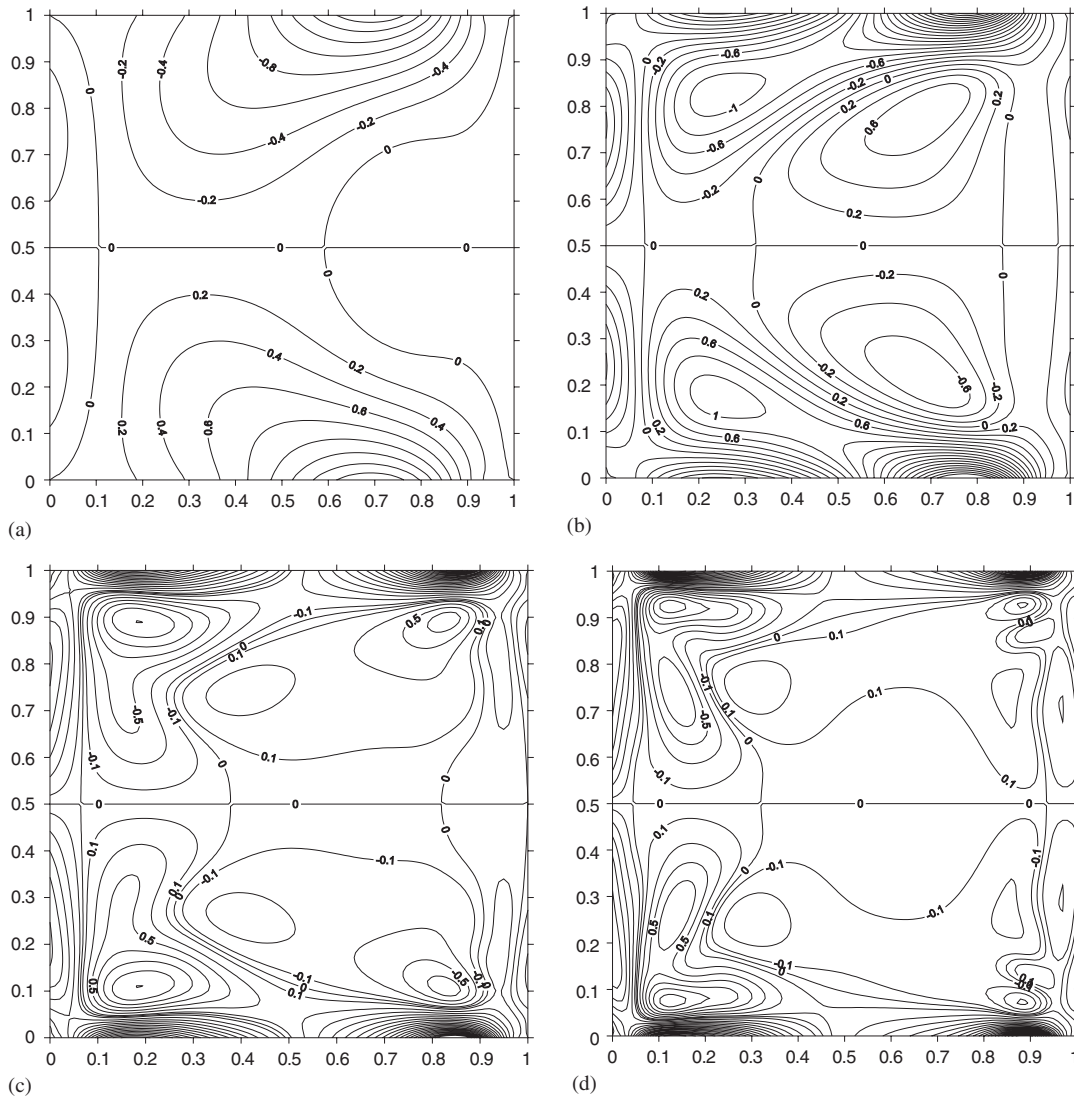


Figure 10. Vorticity (ζ) contour at $z=0.5$ plane. (a) $Re = 100$; (b) $Re = 400$; (c) $Re = 1000$; (d) $Re = 2000$.

served. As the Reynolds number increases, these secondary vortices start moving towards the corners of the cavity due to the end wall effects. These trends are clearly depicted by the above figures with increase in Reynolds number. The approach of these secondary vortices to the extreme corners of the cavity are very clearly observed for $Re = 2000$ as shown in Figure 9(d). The z direction vorticity contours at $z=0.5$ plane are shown in Figures 10(a)–(d). Initially for $Re = 100$, the vortex strength starts appearing only at the upper and bottom downstream regions of the x – y plane. As the Reynolds number increases, the flow takes place in

the z direction also, thus causing the generation of velocity gradients along the other sides of the x - y plane. This results in the formation of vortices originally closer to the initial vortices and these secondary vortices gain more strength and start moving towards the corners as the Reynolds number increases. These flow patterns can be clearly observed from the above figures. In general it is observed that the flow pattern becomes more complex as the Reynolds number increases above 1000.

5. CONCLUSIONS

A finite difference numerical solution procedure for solving three-dimensional Navier–Stokes equations in velocity–vorticity form is tested for a lid-driven cubical cavity flow. The simplified numerical procedure has enabled us the use of a very fine mesh of size $101 \times 101 \times 101$ for numerical predictions of cavity flow up to $Re = 2000$ on a Pentium-IV personal computer. The numerical results obtained for $Re = 100, 400, 1000$ for a typical cubic cavity flow are in good agreement with the results obtained by other numerical schemes. The use of a uniform fine mesh of size $101 \times 101 \times 101$ could predict the complex flow patterns when the Reynolds number is increased to 2000. When parallel computation is the order of the day, the present numerical scheme demonstrates that the finite difference method could be used efficiently for solving high Reynolds number flow problems in three dimensions using a personal computer.

ACKNOWLEDGEMENTS

We acknowledge the financial support from NSC, Taiwan, it is greatly appreciated.

REFERENCES

1. Glowinski R, Pironneau O. Finite element methods for Navier–Stokes equations. *Annual Review of Fluid Mechanics* 1992; **24**:167–204.
2. Fernandez G, Hafez M. Stable finite-element solution of the incompressible Navier–Stokes equations using linear interpolations for velocity and pressure. *Computer Methods in Applied Mechanics and Engineering* 2001; **191**:545–559.
3. Thomasset. *Implementation of Finite Element Methods for the Navier–Stokes Equations*. Springer: Berlin, 1981.
4. Young DL, Huang JL, Eldho TI. Simulation of laminar vortex shedding flow past cylinders using a coupled BEM and FEM model. *Computer Methods in Applied Mechanics and Engineering* 2001; **190**:5975–5998.
5. Young DL, Chang JT, Eldho TI. A coupled BEM and arbitrary Lagrangian–Eulerian FEM model for the solution of two-dimensional laminar flows in external flow fields. *International Journal for Numerical Methods in Engineering* 2001; **51**:1053–1077.
6. Elshabka AM, Chung TJ. Numerical solution of three-dimensional stream function vector components of vorticity transport equations. *Computer Methods in Applied Mechanics and Engineering* 1999; **170**:131–153.
7. Giese JH. Stream functions for three-dimensional flows. *Journal of Mathematical Physics* 1951; **30**(1):31–35.
8. Weinan E, Liu JG. Finite difference methods for 3D viscous incompressible flows in the vorticity-vector-potential formulation on nonstaggered grids. *Journal of Computational Physics* 1997; **138**:57–82.
9. Wong KL, Baker AJ. A 3D incompressible Navier–Stokes velocity–vorticity weak form finite element algorithm. *International Journal for Numerical Methods in Fluids* 2002; **38**:99–123.
10. Young DL, Yang SK, Eldho TI. Solution of the Navier–Stokes equations in velocity–vorticity form using a Eulerian–Lagrangian boundary element method. *International Journal for Numerical Methods in Fluids* 2000; **34**:627–650.
11. Young DL, Liu YH, Eldho TI. A combined BEM-FEM model for the velocity–vorticity formulation of the Navier–Stokes equations in three dimensions. *Engineering Analysis with Boundary Elements* 2000; **24**:307–316.

12. Guj G, Stella F. A vorticity-velocity method for the numerical solution of 3D incompressible flows. *Journal of Computational Physics* 1993; **106**:286-298.
13. Wu XH, Wu JZ, Wu JM. Effective vorticity-velocity formulations for three-dimensional incompressible viscous flows. *Journal of Computational Physics* 1995; **122**:68-82.
14. Giannattasio P, Napolitano M. Optimal vorticity conditions for the node-centred finite-difference discretization of the second-order vorticity-velocity equations. *Journal of Computational Physics* 1996; **127**:208-217.
15. Clercx HJH. A spectral solver for the Navier-Stokes equations in the velocity-vorticity formulation for flows with two nonperiodic directions. *Journal of Computational Physics* 1997; **137**:186-211.
16. Trujillo J, Karniadakis GE. A penalty method for the vorticity-velocity formulation. *Journal of Computational Physics* 1999; **149**:32-58.
17. Goda K. A multistep technique with implicit difference schemes for calculating two- or three-dimensional cavity flows. *Journal of Computational Physics* 1979; **30**:76-95.
18. Guj G, Stella F. Numerical solutions of the high-Re recirculating flows in vorticity-velocity form. *International Journal for Numerical Methods in Fluids* 1988; **8**:405-416.
19. Daube O. Resolution of the 2D Navier-Stokes equations in velocity-vorticity form by means of an influence matrix technique. *Journal of Computational Physics* 1992; **103**:402-414.
20. Lo DC, Young DL. Two-dimensional incompressible flows by velocity-vorticity formulation and finite element method. *Chinese Journal of Mechanics* 2001; **17**(1):13-20.
21. Fasel H. Investigation of the stability of boundary layers by a finite-difference model of the Navier-Stokes equations. *Journal of Fluid Mechanics* 1976; **78**:355-383.
22. Orlandi P. Vorticity-velocity formulation for high Re flows. *Computers and Fluids* 1987; **15**:137-149.
23. Liu CH. Numerical solution of three-dimensional Navier-Stokes equations by a velocity-vorticity method. *International Journal for Numerical Methods in Fluids* 2001; **35**:533-557.
24. Napolitano M, Pascazio G. A numerical method for the vorticity-velocity Navier-Stokes equations in two and three dimensions. *Computer and Fluids* 1991; **19**:489-495.
25. Guevremont G, Habashi WG, Hafez MM. Finite element solution of the Navier-Stokes equations by a velocity-vorticity method. *International Journal for Numerical Methods in Fluids* 1990; **11**:661-675.
26. Mallinson G, de Vahl Davis G. The method of the false transient for the solution of coupled elliptic equations. *Journal of Computational Physics* 1973; **12**:435-461.
27. Napolitano M, Catalano LA. A multigrid solver for the vorticity-velocity Navier-Stokes equations. *International Journal for Numerical Methods in Fluids* 1991; **13**:49-59.
28. Batchelor GK. *Introduction to Fluid Dynamics*. Cambridge University Press: Cambridge, 1967.
29. Jiang BN, Lin TL, Povinelli LA. Large-scale computation of incompressible viscous flow by least-squares finite element method. *Computer Methods in Applied Mechanics and Engineering* 1994; **114**:213-231.
30. Shu C, Wang L, Chew YT. Numerical computation of three-dimensional incompressible Navier-Stokes equations in primitive variable form by DQ method. *International Journal for Numerical Methods in Fluids* 2003; **43**:345-368.
31. Nikfetrat K, Hafez M. Three dimensional viscous incompressible flow simulations using Helmholtz velocity decomposition. *Computational Fluid Dynamics Journal* 2002; **10**(4):439-445.
32. Ho CJ, Lin FH. Numerical simulation of three-dimensional incompressible flow by a new formulation. *International Journal for Numerical Methods in Fluids* 1996; **23**:1073-1084.
33. Ku HC, Hirsh RS, Taylor TD. A pseudospectral method for solution of the three-dimensional incompressible Navier-Stokes equations. *Journal of Computational Physics* 1987; **70**:439-462.
34. Burggraf OR. Analytic and numerical studies of structure of steady separated flows. *Journal of Fluid Mechanics* 1966; **24**:131-151.
35. Ghia U, Ghia KN, Shin CT. High-Re solutions for incompressible flow using the Navier-Stokes equations and a multigrid method. *Journal of Computational Physics* 1982; **48**:387-411.